Acoustic energy dissipation and thermalization in carbon nanotubes: Atomistic modeling and mesoscopic description

William M. Jacobs,[*] David A. Nicholson,[†] Hagit Zemer, Alexey N. Volkov, and Leonid V. Zhigilei[‡]

Department of Materials Science and Engineering, University of Virginia, USA

The exchange of energy between low-frequency mechanical oscillations and high-frequency vibrational modes in carbon nanotubes (CNTs) is a process that plays an important role in a range of dynamic phenomena involving the dissipation of mechanical energy in both individual CNTs and CNT-based materials. The rates and channels through which acoustic energy deposited instantaneously in individual CNTs is dissipated are investigated in a series of atomistic molecular dynamics simulations. Several distinct regimes of energy dissipation, dependent on the initial stretching or bending deformations, are established. The onset of axial or bending buckling marks the transition from a regime of slow thermalization to a regime in which the energy associated with longitudinal and bending oscillations is rapidly damped. In the case of stretching vibrations, an intermediate regime is revealed in which dynamic coupling between longitudinal vibrational modes and the radial "squash" mode causes delayed axial buckling followed by a rapid transfer of energy to high-frequency vibrations. The results of the atomistic simulations are used in the design and parameterization of a "heat bath" description of thermal energy in a mesoscopic model, which is capable of simulating systems consisting of thousands of interacting CNTs. Two complementary methods for the description of mechanical energy dissipation in the mesoscopic model are developed. The relatively slow dissipation of acoustic vibrations in the absence of buckling is described by adding a damping force to the equations of motion of the dynamic elements of the mesoscopic model. The sharp increase in the energy dissipation rate at the onset of buckling is reproduced by incorporating a hysteresis loop into the strain energy that accounts for localized thermalization in the vicinity of buckling kinks. The ability of the mesoscopic model to reproduce the complex multistep processes of acoustic energy dissipation predicted by the atomistic simulations is demonstrated in mesoscopic simulations of free stretching and bending vibrations of individual CNTs.

I. INTRODUCTION

Current interest in carbon nanotube (CNT)-based materials is fueled by a broad range of potential applications, ranging from the fabrication of flexible/stretchable electronic and acoustic devices to the design of advanced nanocomposite materials with improved toughness, resistance to blast/impact loading and fire-retardant properties.[1–3] Despite the rapid development of new CNT materials, computational efforts in this area have been limited by a lack of models capable of adequately describing the collective dynamics of large groups of CNTs that define the behavior and properties of nanofibrous materials, such as CNT films, mats, and buckypaper. Depending on the structure of the material and the phenomenon of interest, the number of individual CNTs that must be included in the representative volume element of the material in order to predict the effective (macroscopic) material properties can range from several hundreds to millions. Since the direct atomic-level simulation of systems consisting of large groups of CNTs is beyond the capabilities of modern computing facilities, the application of atomistic modeling is typically limited to the investigation of individual nanotubes or small groups consisting of up to several tens of relatively short (usually tens of nanometers) CNTs.[4–6]

The recent development of coarse-grained (or mesoscopic) models based on grouping atoms into larger dynamic units[7–10] has provided an attractive alternative to the direct atomistic modeling of CNTs. In particular, a mesoscopic model that represents individual CNTs as chains of stretchable cylindrical segments[7] has been demonstrated to be capable of simulating systems consisting of thousands of interacting CNTs on time scales extending up to tens of nanoseconds.[8,11] Previous simulations performed with this mesoscopic model have revealed the driving forces responsible for the spontaneous self-organization of CNTs into continuous networks of bundles[8] and have identified CNT bending buckling as an important factor that limits the coarsening of network structures and ensures their stability.[11] The mesoscopic model has also been adapted for calculating the thermal transport properties of CNT network structures.[12–14]

In order to exploit the dynamic nature of the mesoscopic model for simulating CNT-based materials under conditions of fast mechanical loading (e.g., blast/impact resistance or response to shock loading), it is necessary to incorporate a description of energy dissipation into the model. Figure 1 illustrates the existing mesoscopic model's ability to simulate the high-velocity (1000 m/s) impact of a spherical projectile on a free-standing thin CNT film, albeit without accounting for the dissipation of mechanical energy—a deficiency that significantly affects the simulation's accuracy. While the coarse-grained representation of CNTs reduces the number of degrees of freedom that must be tracked in calculations and greatly increases the time and length scales of the simulations, it also introduces a cutoff frequency above which bending and stretching vibrations cannot be resolved. Moreover, the model does not account for twisting, radial, and optical vibrational modes[15] and grossly underestimates the heat capacity of the material. The absence of high-frequency
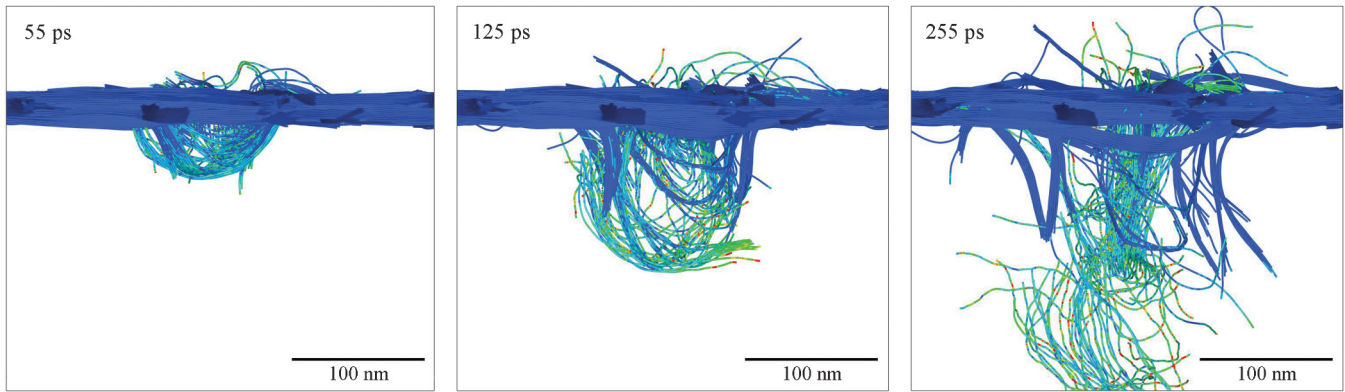
FIG. 1. (Color online) Snapshots from a mesoscopic simulation of the high-velocity impact of a spherical projectile with a diameter of 100 nm, a density of 2.8 g/cm^3 and an initial velocity of 1000 m/s on a free-standing 20-nm-thick CNT film. The snapshots are shown for 55, 125, and 255 ps after the onset of the impact. The film has a density of 0.2 g/cm^3, and the CNTs in the film are arranged in a continuous network of bundles. The nanotubes are colored by their local kinetic energy, and the projectile is not shown in the snapshots.

vibrational modes prevents dissipation of the kinetic energy into the internal energy of the CNTs, leading to a fast increase in the "temperature" associated with the dynamic degrees of freedom of the model in dynamic simulations conserving the total energy. In simulations of slowly evolving systems, local thermal equilibrium (i.e., equipartition of thermal energy among the collective dynamic degrees of freedom that are explicitly represented in the model and the internal degrees of freedom associated with the vibrational modes that are not present in the model) can be assumed, and temperature control can be used to avoid large temperature variations associated with the structural evolution of the system.[8,10,11] The assumption of local thermal equilibrium is not valid, however, in simulations of dynamic phenomena occurring far from thermal equilibrium, as in the case of the impact-driven mechanical loading illustrated in Fig. 1.

In order to enable mesoscopic simulations of dynamic phenomena, it is necessary to design an adequate computational description of the energy exchange between the vibrational modes that are represented in the coarse-grained mesoscopic model and those that are omitted. A general solution is to include the energy of the vibrational modes that are missing in the mesoscopic model through internal "heat bath" variables associated with the dynamic elements of the model and to allow for energy exchange between the dynamic degrees of freedom and the heat bath variables. This general approach has been implemented to describe energy exchange between the electrons and phonons in metals[16] and between the translational and intramolecular motions in molecular systems.[17,18] It has enabled simulations under conditions of strong non-equilibrium between the dynamic degrees of freedom and the internal heat bath variables, which can be created by shock loading,[18] or by short-pulse laser excitation of conduction band electrons in metals[16] or internal vibrational states in molecular systems.[17] In all of these examples, there is a clear physical distinction and/or a large separation in frequency space between the dynamic vibrational modes and the subsystem represented by the heat bath. As a result, distinct internal and dynamic temperatures may be introduced, and it is possible to reproduce a predefined rate of thermal equilibration between the internal and dynamic

degrees of freedom by adding dissipative terms to the equations of motion describing the dynamic elements of the model.

In the case of CNTs, a physical distinction between the low-frequency acoustic vibrational modes represented in the mesoscopic model and the remaining degrees of freedom is not as apparent. Nevertheless, the results of recent atomic-level molecular dynamics (MD) simulations provide justification for splitting the frequency domain into distinct low- and high-frequency regions. In particular, simulations of heat transfer between CNTs and surrounding octane[19,20] and argon[21] matrices suggest that the energy exchange between low-frequency vibrational modes, which readily equilibrate with the matrices, and high-frequency modes, which make the greatest contribution to the heat capacity of the CNTs, is slow and is limited by a weak coupling between the acoustic and optical vibrational modes. This observation has motivated the discussion of the thermal equilibration process in terms of the evolution of distinct spectrally resolved temperatures reflecting the level of thermal excitation of particular vibrational modes or frequency domains.[19,21] The relatively slow dissipation of bending oscillations in cantilevered,[22,23] free,[24] and clamped[25] (by periodic boundary conditions) CNTs also supports the notion of weak coupling (or the presence of a "phonon bottleneck"[25]) between the excited acoustic vibrations and the rest of the vibrational modes. These observations of slow energy exchange between the high- and low-frequency vibrations provide a solid foundation for describing the high-frequency vibrational modes in the mesoscopic model within the general framework of the heat bath approach.

In order to design and parameterize a heat bath for the mesoscopic model of CNTs, it is necessary to establish two quantities: the heat capacity of the bath and the rate of energy transfer between the vibrational modes that are explicitly represented in the mesoscopic model and those that are approximated by the heat bath. The former quantity can be easily obtained by subtracting the contribution of the dynamic degrees of freedom from the experimental specific heat of CNTs which, at and above room temperature, can be safely derived from measurements performed for CNT bundles or crystalline graphite.[26,27] For the purpose of

comparing the predictions of the mesoscopic model with the results of classical MD simulations, the heat capacity can also be obtained theoretically, using the equipartition and virial theorems of classical mechanics. The rates of energy transfer between the mechanical vibrations of CNTs and their high-frequency vibrational modes, however, have only been investigated in a limited number of atomic-level MD simulations[22–25] performed in the context of energy dissipation in CNT oscillators. The complete picture of the dependence of the rate of energy dissipation on the internal CNT temperature and the initial energy of the excited vibrational modes has not yet been established.

In this paper, we report the results of atomic-level MD simulations of acoustic energy dissipation in a single free CNT with different levels of initial stretching or bending deformation. Several regimes of energy dissipation are established, and the results of the simulations are suitably formulated for implementation in the mesoscopic model. The heat bath approach for describing the thermal energy of the nanotubes is then developed and tested for free vibrations of individual CNTs.

II. ATOMISTIC SIMULATIONS

A. Computational model and analysis of energy dissipation

The atomistic MD simulations were performed with 26-nm-long (10,10) single-walled CNTs composed of 4 260 atoms arranged into 100 unit-cell rings (40 atoms per unit cell) and two 130-atom caps. Each cap consists of one half of a C^{240} fullerene molecule, which interfaces with the nanotube by a 10-atom ring. The interatomic interactions are described by the adaptive intermolecular reactive empirical bond-order (AIREBO) potential.[28] The simulations of free stretching and bending vibrations of CNTs were performed under the condition of constant total energy, making it possible to follow the dissipation of the mechanical energy deposited in the acoustic modes at the beginning of the simulations.

All nanotubes were initially equilibrated at temperatures of 41, 294, 568, and 1054 K. The equilibrated CNTs were instantaneously deformed by either homogeneously stretching or bending the nanotubes at the beginning of the simulations of free vibrations (this time corresponds to the time $t = 0$ in the discussion of the results in Secs. II B and II C). In the case of axial stretching, the initial tensile strain was varied between 0.5% and 10%, with the maximum values exceeding the proportional strain limit but not surpassing the yield strain.[29] In the case of the bending deformation, the positions and velocities of the atoms were transformed so that CNT deforms into an arc with a constant radius of curvature while preserving both the length of the centerline of the CNT and the relative angles between the atomic velocity vectors and the centerline. The simulations were performed for radii of curvature ranging from 10 to 1000 nm. This range includes radii that are both below and above the critical value for the onset of bending buckling determined in quasistatic simulations of (10,10) CNTs, approximately 27 nm.[11,30,31]

The analysis of the energy flow from the low-frequency acoustic modes excited at the beginning of the simulations to other vibrational modes is based on the partitioning of the total energy of a nanotube into energies associated with four distinct groups of vibrational modes: the longitudinal acoustic (LA) modes, the bending acoustic (BA) modes, an approximate representation of radial modes (Rad) associated with changes in the nanotube cross sections, and the remaining "heat bath" (HB) modes that include the high-frequency optical as well as the acoustic twist modes. This partitioning allows for a direct mapping of the results of the atomistic simulations onto a description of energy dissipation in the mesoscopic model, in which only the low-frequency longitudinal and bending vibrations are represented explicitly.[7,8,11] The total energy of the missing vibrational modes in the mesoscopic model is accumulated in heat bath variables that are coupled to the dynamic degrees of freedom (see Sec. III). The radial modes are not explicitly represented in the current version of the mesoscopic model, but are distinguished in the analysis of the MD simulation results in order to obtain a clearer picture of the physical mechanisms responsible for the transitions between different regimes of energy dissipation. Some of the radial modes can be included in the mesoscopic simulations by adding the local CNT radii to the set of dynamic variables.[7,8]

In the evaluation of the energy associated with the longitudinal and bending acoustic modes of a CNT, the center of mass positions and velocities of all unit cell rings are first calculated by averaging over the corresponding 40 carbon atoms in each cell. The acoustic modes of the CNT can then be analyzed in a manner consistent with the mesoscopic representation of the CNT as a chain of coarse-grained particles (or nodes). Each node represents a cylindrical segment with length equal to the axial size of the unit cell. The effect of the two half fullerene caps on the dynamics of the nanotube is neglected in the analysis. The correspondence between the atomistic model of a CNT and its mesoscopic representation is illustrated in Fig. 2(a). Note that the length of a CNT segment in the mesoscopic model does not have to be equal to the length of a CNT unit cell and is substantially longer in actual mesoscopic simulations.[7,8,11,12] The mesoscopic segment length is chosen to be equal to the CNT unit cell length in the analysis of the atomistic simulation results in order to ensure that all LA and BA modes are accounted for and that the corresponding energies associated with these groups of modes are reproduced.

In order to measure the instantaneous energy associated with a distinct group of vibrational modes, it is necessary to calculate both the kinetic and potential energy contributions from this group of modes. In accordance with the mesoscopic model, the total (harmonic) potential energies associated with LA and BA modes are

$$U_{\text{LA}} = \frac{1}{2}\frac{k_{\text{str}}}{a}\sum_{i=1}^{N-1}(|\vec{r}^{\,i+1} - \vec{r}^{\,i}| - a)^2 \tag{1}$$

and

$$U_{\text{BA}} = \frac{1}{2}k_{\text{bnd}}a\sum_{i=2}^{N-1}\left(\frac{1}{R_i}\right)^2, \tag{2}$$

respectively, where $\vec{r}^{\,i}$ is the position of node i, a is the equilibrium separation between the nodes (the length of a CNT segment in the mesoscopic model), k_{str} and k_{bnd} are the stretching and bending force constants,[7] respectively, and R_i is the local radius of curvature at node i. The corresponding
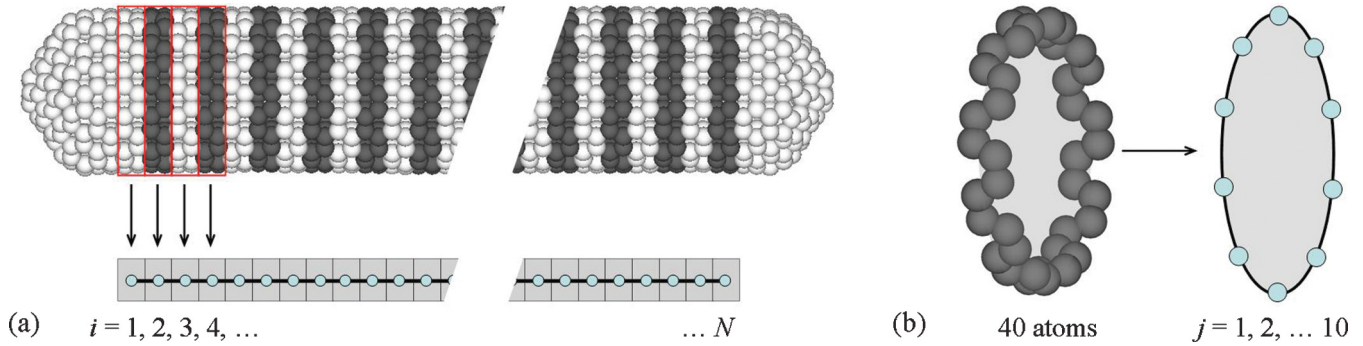
FIG. 2. (Color online) Schematic illustration of the mapping of (a) the atomistic model of a (10,10) CNT to a chain of coarse-grained particles and (b) a unit cell ring of the (10,10) CNT to a closed chain of 10 point masses. The coarse-grained representations are used in the analysis of the partitioning of the vibrational energy between the longitudinal, bending, and radial modes of the CNT.

kinetic energies of the LA and BA modes can be determined from the components of the node velocities $\vec{v}^i$ parallel and perpendicular, respectively, to the local elastic line defined as $\vec{e}^i = (\vec{r}^{i+1} - \vec{r}^{i-1})/|\vec{r}^{i+1} - \vec{r}^{i-1}|$ for internal nodes and as a line directed along the two end segments for nodes $i = 1$ and N:

$$T_{\mathrm{LA}} = \frac{1}{2} m \sum_{i=1}^{N} (\vec{v}^i \cdot \vec{e}^i)^2 \qquad (3)$$

and

$$T_{\mathrm{BA}} = \frac{1}{2} m \sum_{i=1}^{N} [(\vec{v}^i)^2 - (\vec{v}^i \cdot \vec{e}^i)^2], \qquad (4)$$

where $m = 40 \times 12$ amu $= 480$ amu is the total mass of each node.

Direct application of Eqs. (1) and (3) gives a satisfactory estimate of the total LA energy, $E_{\mathrm{LA}} = T_{\mathrm{LA}} + U_{\mathrm{LA}}$, subject to the correct choice of the temperature-dependent node separation a [the AIREBO potential predicts an expansion of the length of a (10,10) CNT by 0.3% as the temperature changes from 40 to 1054 K]. The dependence of a on the instantaneous HB temperature θ is determined from the average node spacing in equilibrium MD simulations and is used in the dynamic stretching and bending simulations. Since the time-averaged values of kinetic and potential energies of the LA modes are equal within the harmonic approximation, it is possible to calculate an appropriate prefactor $[k_{\mathrm{str}}/(2a)]$ for the LA potential energy empirically by requiring the time integral of the LA potential energy to be equal to that of the LA kinetic energy, and thus to avoid calculating the temperature-dependent force constant k_{str} directly. Given that the number of heat bath modes is far greater than the number of longitudinal and bending modes, the dissipation of energy from the excited mechanical vibrations results in a moderate increase in the heat bath temperature during the simulation, and a single value of the scaling factor is chosen for each simulation.

In the analysis of the BA modes, the precise definitions of the local radius of curvature and the number of neighboring nodes included in the calculation significantly affect the bending potential energy. When only nearest-neighbor nodes are considered, the direct application of Eq. (2) does not yield

the periodic fluctuations that are expected for large-amplitude bending oscillations. In this case, a normal mode analysis, which measures small bending oscillations relative to a fixed axis, more appropriately captures the collective dynamics of low-frequency bending oscillations. The total BA potential energy is reconstructed from the sum of the energies contained in each of the mesoscopic normal modes denoted by ρ_{BA}, the eigenstates of the mesoscopic system. Given free boundary conditions, the BA potential energy calculated according to this mode analysis is

$$U_{\mathrm{BA}} = \frac{1}{2} m \sum_{s=1}^{N-1} [\omega_{\mathrm{BA}}^{(s)}]^2 \left\{ \left[\sum_{i=1}^{N} (r_x^i - r_{x,0}^i) \rho_{\mathrm{BA}}^{(s),i} \right]^2 \right.$$
$$\left. + \left[\sum_{i=1}^{N} (r_y^i - r_{y,0}^i) \rho_{\mathrm{BA}}^{(s),i} \right]^2 \right\}, \qquad (5)$$

where

$$\rho_{\mathrm{BA}}^{(s),i} = \cos \left[\frac{s\pi(i - 1/2)}{N} \right] \qquad (6)$$

and

$$[\omega_{\mathrm{BA}}^{(s)}]^2 = \frac{16 k_{\mathrm{bnd}}}{ma^3} \sin^4 \left(\frac{s\pi}{2N} \right), \qquad (7)$$

with k_{bnd} scaled analogously to k_{str} in order to match the time-averaged kinetic and potential energies. The positions and velocities of nodes, (r_x^i, r_y^i, r_z^i) and (v_x^i, v_y^i, v_z^i), are the center of mass positions and velocities of a unit cell ring i in Cartesian coordinates. The z axis is directed along the axis of the equilibrated (deformation-free) nanotube defined by nodes $(r_{x,0}^i, r_{y,0}^i, r_{z,0}^i)$. Since the distribution of the atomic velocities prior to equilibration of the CNTs introduces small nonzero angular momenta, a transformation is applied to the atomic positions and velocities such that the CNT is reoriented along the z axis prior to the analysis of the results at a given time step. Although the normal mode analysis given by Eqs. (5)–(7) is only valid in the limit of small displacements of the nodes, we find that the use of Eqs. (4) and (5) minimizes the oscillations of the total energy of the BA modes, $E_{\mathrm{BA}} = T_{\mathrm{BA}} + U_{\mathrm{BA}}$, in equilibrium simulations and results in a smooth profile for E_{BA} in dynamic bending simulations. The summation in Eq. (5) is performed over nodes i and doubly degenerate normal bending modes s corresponding to the displacements in two orthogonal

(x and y) transverse directions. The lowest normal mode, $s = 0$, corresponds to linear translation of the entire CNT and is excluded from the calculations since the net linear momentum is ignored; this observation also applies to the LA modes. As a consequence, in simulations consisting of 100 unit cell rings, the analysis described above accounts for the contribution of 99 LA and 198 BA modes.

Although radial modes are not currently included in the mesoscopic description, a separate treatment of the radial mode energy is important in the analysis of the MD results. To obtain a measure of the energy transferred to the radial modes of an armchair (10,10) CNT, we approximate the structure of a unit cell ring by a closed chain of $n = 10$ particles (point masses). Each particle corresponds to four atoms of the unit cell [a part of a hexagon, as shown in Fig. 2(b)]. By considering the radial velocities of the particles, the total radial kinetic energy of all rings in the nanotube can be calculated as

$$T_{\text{Rad}} = \frac{1}{2} \frac{m}{n} \sum_{i=1}^{N} \sum_{j=1}^{n} \left(v_{R,j}^{i} \right)^2, \qquad (8)$$

where $v_{R,j}^{i}$ is the radial component of the velocity of particle j in unit cell ring i with respect to the center of mass of the ring. We can obtain a smooth energy profile by calculating a moving average of $T_{\text{Rad}}(t)$ with a time window equal to the period of breathing oscillations, approximately 1 ps. By invoking the virial theorem, we can approximate the total radial energy as $E_{\text{Rad}} = 2T_{\text{Rad}}$.

The radial kinetic energy of each ring can be further decomposed into contributions from n radial modes. Because of the periodicity of the ring, we can approximate the radial kinetic energy of ring i contained in mode s as

$$T_{\text{Rad}}^{i,(s)} = \frac{1}{2} \frac{m}{n} \left[\sum_{j=1}^{n} v_{R,j}^{i} \rho_{\text{Rad}}^{(s),j} \right]^2, \qquad (9)$$

where

$$\rho_{\text{Rad}}^{(s),j} = \begin{cases} \cos\left(\frac{2\pi s j}{n} \right), & s = 0,1,\ldots,\left(\frac{n}{2} - 1 \right) \\ \sin\left(\frac{2\pi s j}{n} \right), & s = 1,2,\ldots,\frac{n}{2} \end{cases} . \qquad (10)$$

The summation in Eq. (9) is performed over n particles in unit cell ring i. Since the center of mass velocities of the rings are eliminated in the analysis, each ring has $n - 1$ radial degrees of freedom. With $N = 100$ and $n = 10$, the number of radial modes revealed in this analysis is $N(n - 1) = 900$. The radial modes with $s = 0$ and $s = 2$ correspond to the radial breathing and squashing oscillations of the nanotube cross sections, respectively. Although this approximate representation of the radial modes does not account for all radial modes present in the CNT, it allows us to follow the flow of energy to this group of vibrational modes and, in particular, to identify the excitation of the "squash" mode as a precursor for axial buckling (see Sec. II B).

Lastly, the energy of the remaining (heat bath) vibrational modes is calculated by subtracting the sum of the total energies associated with the longitudinal, bending, and radial modes from the total energy of the nanotube,

$$E_{\text{HB}} = E_{\text{CNT}} - (E_{\text{LA}} + E_{\text{BA}} + E_{\text{Rad}}). \qquad (11)$$

Since the 130-atom caps at the ends of the nanotube are neglected in the analysis of the LA, BA, and Rad modes, the energy of the atoms belonging to the caps is also excluded in the calculation of E_{CNT}. With this definition, and taking into account that the translational motion of the entire nanotube is eliminated in the simulations, the heat bath is comprised of a total of 10 800 distinct vibrational modes (3 × 4000 atoms – 99 LA – 198 BA – 900 Rad – 3 translational).

Ten simulations, each of which was initialized from a unique configuration of atomic positions and velocities, were conducted for each combination of initial strain and initial temperature. The rates of thermalization of stretching and bending oscillations were determined by dividing the duration of the atomistic simulations into discrete time intervals.[32] For each interval, the decay rate of the energy associated with the excited group of vibrational modes was calculated by linear regression. Associated average values for the longitudinal, bending, radial, and heat bath energies were also determined at the midpoint of each time interval. The values of energy were converted to temperature units for each group of modes by dividing the energy values by the product of the corresponding number of modes present in each group and the Boltzmann constant k_B, e.g., $\theta_{\text{LA}} = E_{\text{LA}}/(99k_B)$. The conversion of the energy values to temperature units does not imply an assumption of thermal equilibrium, but simply provides a convenient way to compare the instantaneous energy values for different groups of vibrational modes with drastically different numbers of degrees of freedom.

B. Dissipation of LA mode vibrations

The analysis of the rates and mechanisms of the energy transfer from LA modes excited at the beginning of the simulations to the other vibrational modes reveals the existence of three distinct regimes of stretching energy dissipation. The evolution of the energies of the LA, BA, Rad, and HB modes characteristic of these three regimes is shown for simulations performed with different values of initial strain in Fig. 3. In the first regime *(stretching regime I)*, at low initial strain [e.g., Fig. 3(a)], a smooth, gradual decay of the energy of LA oscillations is observed on the time scale of hundred(s) of picoseconds. In the second regime *(stretching regime II)*, at intermediate initial strains of about 3.2–5% [e.g., Fig. 3(b)], a more complex three-step energy transfer resulting from radial mode-mediated axial buckling is observed. Finally, in the third regime *(stretching regime III)*, at high initial strain [e.g., Fig. 3(c)], an immediate thermalization of most of the stretching energy takes place due to the compressive axial buckling of the nanotube. The rates of mechanical energy dissipation and the pathways of the energy redistribution among the vibrational modes are discussed next for each of these three regimes.

The gradual decay of the energy of the excited LA modes shown in Fig. 3(a) is typical of simulations performed with initial strains of 3% and below. Following the excitation of the LA modes, the length of the CNT begins oscillating with a frequency of the lowest LA mode, approximately 0.3 THz. The amplitude of these oscillations decreases with time, as the deposited energy is transferred to the BA, Rad, and HB modes due to dynamic coupling between the vibrational modes. The
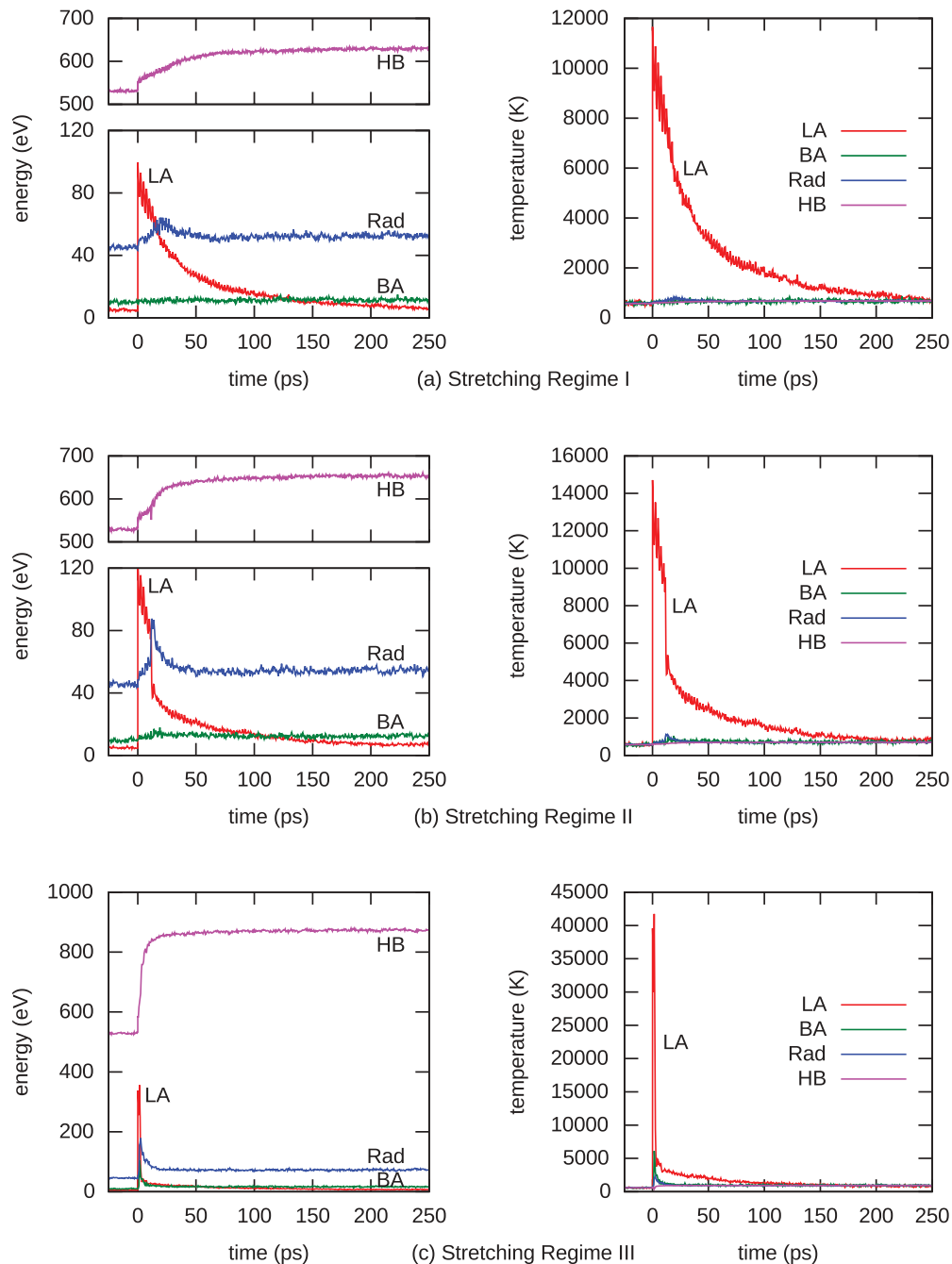
FIG. 3. (Color online) The evolution of the energies of the LA, BA, Rad, and HB modes in simulations performed for CNTs equilibrated at a temperature of 568 K and homogeneously stretched at time $t = 0$ with initial axial strains of 3% (a), 4% (b), and 6% (c). In the right panels, the values of energy are converted to temperature units for each group of modes by dividing the energy values by the product of the corresponding number of modes present in each group and the Boltzmann constant. These three simulations represent the three distinct regimes of stretching energy dissipation identified in the simulations.

energy transfer results in the thermalization of the CNT, with the effective "temperatures" of each of the groups of modes converging towards thermal equilibrium [see the right panel of Fig. 3(a)]. The energy plots shown in the left panels of Fig. 3(a) indicate that most of the energy of the excited LA modes is transferred to the HB modes, which are primarily comprised of high-frequency optical modes and have an almost ten times greater heat capacity than the combined LA, BA, and Rad modes. A strong dynamic coupling between the stretching

oscillations and the radial modes can also be noted in the energy plots. This coupling plays the key role in causing the transition to the second regime of the energy dissipation at higher axial strains.

The rate of decay of the energy of the LA oscillations in the simulations performed in stretching regime I, in which the initial axial strain does not exceed 3%, is largely defined by the temperature of the CNT and the level of the stretching excitation. The temperature and strain dependencies
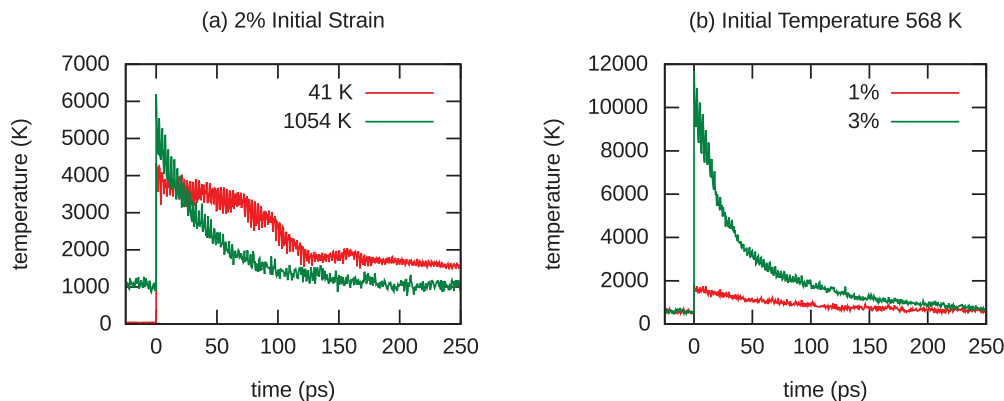
FIG. 4. (Color online) The evolution of the energy (converted to temperature units as explained in the text) of the LA modes in simulations performed for initial temperatures of 41 and 1054 K with the same axial strain of 2% (a) and for initial strains of 1% and 3% at the same initial temperature of 568 K (b).

are illustrated in Fig. 4, where the energy profiles (converted to temperature units as discussed above) are shown for two different values of the initial temperature [see Fig. 4(a)] and strain [see Fig. 4(b)]. It is apparent that higher initial temperatures and/or strains result in faster energy transfer from the excited LA modes. In the quantitative analysis of the rate of energy transfer from the LA modes, this rate is evaluated as a function of the instantaneous temperature θ of the HB modes (these modes account for approximately 90% of all vibrational modes in a CNT, and θ can be used as a measure of the overall temperature of the CNT) and the instantaneous excess energy in the LA modes (the difference between the instantaneous LA energy and the equilibrium value E_{LA}^{θ} corresponding to the instantaneous temperature θ, $E_{LA}^{\theta} = 99 k_B \theta$). Each simulation produces time-dependent decay rates with a range of values corresponding to the variation of the excess energy in the LA modes, $E_{LA} - E_{LA}^{\theta}$, and the temperature θ along the simulated trajectories.

The results of the calculation of the decay rates obtained in simulations performed for four initial temperatures of 41, 294, 568, and 1054 K and four axial strains of 0.5, 1, 2, and 3% are shown in Fig. 5. The decay rate exhibits a strong dependence on the excess energy in the LA modes and approaches zero in the limit of thermal equilibrium. The dependence on the HB temperature is somewhat weaker but still apparent from the plots, with higher rates of thermalization observed at elevated temperatures. The decay rates vary slightly across simulations differing only in their initial atomic configurations, resulting in the sizable error estimates in Fig. 5; however, these path dependencies must be ignored in order to translate the results into a form suitable for implementation in the mesoscopic model. In this first stretching regime, the simulation-averaged decay rates can be relatively well described by the following two-dimensional function of the relative excess energy $(E_{LA} - E_{LA}^{\theta})/E_{LA}^{\theta}$ and the equilibrium energy E_{LA}^{θ} used as a measure of the instantaneous temperature θ:

$$\frac{d}{dt}\left(E_{LA} - E_{LA}^{\theta}\right) = -\gamma^{LA}\left(\frac{E_{LA} - E_{LA}^{\theta}}{E_{LA}^{\theta}}\right)^{\alpha^{LA}}\left(E_{LA}^{\theta}\right)^{\beta^{LA}},$$

(12)

where the best fits for the adjustable parameters are

$$\gamma^{LA} = (1.67 \pm 0.41) \times 10^{-3}\left(eV^{1-\beta^{LA}}ps^{-1}\right),$$

$$\alpha^{LA} = 1.34 \pm 0.07, \text{ and } \beta^{LA} = 2.09 \pm 0.10.$$

The fact that α^{LA} is greater than unity indicates that the dependence of the rate of energy transfer on the instantaneous excess energy in the LA modes is stronger than exponential decay.

The gradual decay of stretching oscillations described by Eq. (12) is only observed in simulations performed with initial strains not exceeding 3–4%. At higher initial strains, a transition to stretching regime II takes place, in which the energy transfer from the excited LA modes proceeds in three distinct steps, as illustrated in Fig. 3(b). The initial gradual energy dissipation, similar to the one in stretching regime I discussed above, suddenly gives way to a sharp drop of the
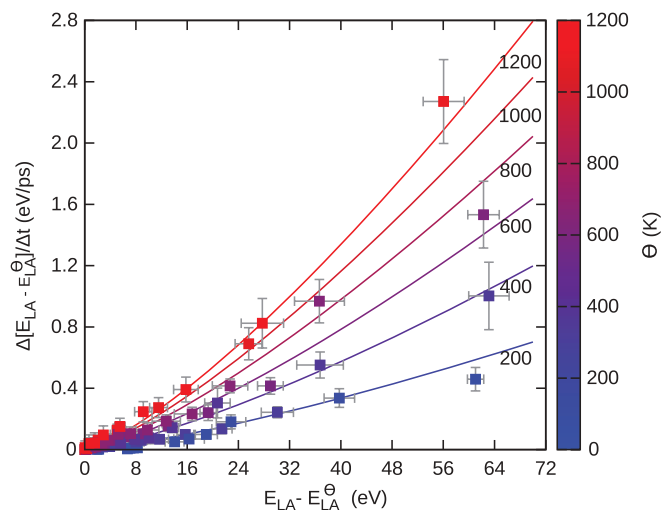

FIG. 5. (Color online) The rate of energy dissipation from the LA modes in the first stretching regime (initial strain does not exceed 3%) as a function of the excess LA energy. The data points are obtained by averaging over ten simulations performed for each combination of initial strain and initial temperature. Isothermal contours of the fitted two-dimensional function given by Eq. (12) are drawn for several temperatures ranging from 200 to 1200 K.
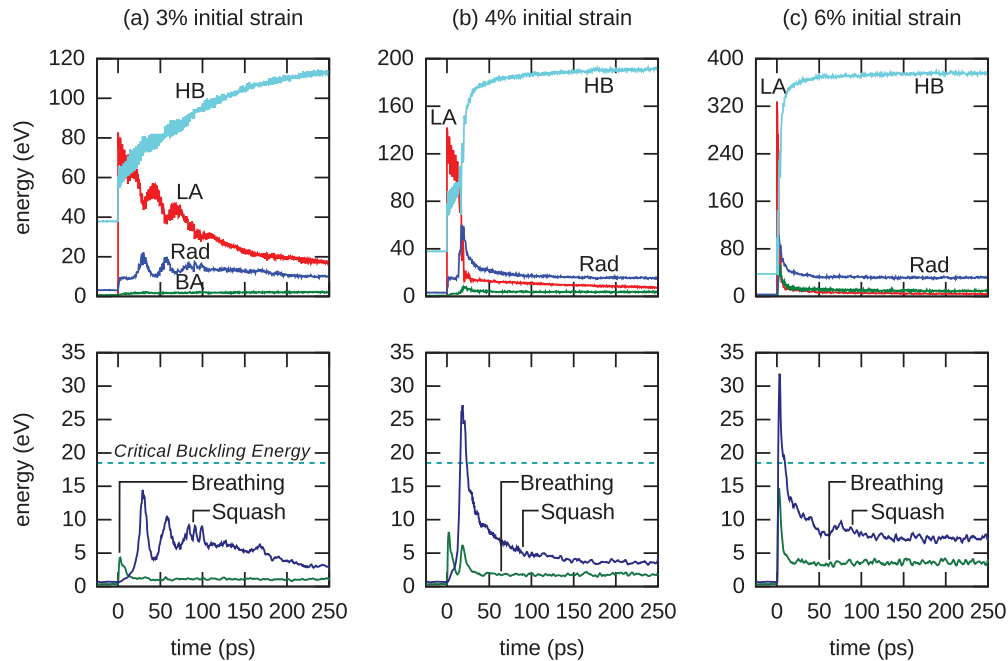
FIG. 6. (Color online) The evolution of the energies of the LA, BA, Rad, and HB modes as well as the radial breathing and squash modes in simulations performed for a CNT equilibrated at a temperature of 41 K and homogeneously stretched at time $t = 0$ with initial axial strains of 3% (a), 4% (b), and 6% (c). The horizontal dashed lines mark the critical value of the second radial mode energy required for the onset of axial buckling.

LA energy corresponding to a rapid thermalization of a large fraction of the initial stretching energy. This drop is followed by a gradual dissipation of the remaining energy of the LA modes that is well described by Eq. (12).

A detailed mode-resolved analysis of the energy redistribution in stretching regime II reveals that the onset of axial buckling, mediated by the excitation of the second radial mode, is responsible for the drop in the energy of the LA modes. The role of the second radial mode in the transition from the first to the second regime of stretching energy dissipation is evident from the energy plots shown in Fig. 6. The simulation illustrated by Fig. 6(a) is performed with an initial axial strain of 3%, just below the level of strain that causes the transition to the second energy dissipation regime. Although the initial stretching of the CNT directly excites the first (breathing) radial mode, the energy of this mode quickly decays and is surpassed by the energy of the second (squash) radial mode, which rises steadily during the first 20 ps after the excitation. Strong dynamic coupling between the LA modes and the second radial mode becomes apparent when the energy of the second radial mode approaches about 15 eV [see Fig. 6(a)]. This dynamic coupling, which is more pronounced in simulations performed at lower temperatures, reversibly transfers energy between the LA modes and the second radial mode, although the overall dissipation of the energy of the excited LA modes can still be described by Eq. (12).

When the excess energy of the second radial mode reaches a critical value of 18.5 ± 0.5 eV, oscillations in the distance between the opposing walls of the CNT that correspond to this mode [see Fig. 7(a)] become unstable, and the CNT buckles axially [see Fig. 7(b)]. Although the deformation of the CNT walls at an axial buckling kink is reversible, the

buckling kink forms a region in which acoustic phonons are effectively scattered, leading to the rapid thermalization of a large portion of the energy contained in the excited LA modes. The amount of energy dissipated as a result of axial buckling varies stochastically between 50 and 75% of the total excess energy of the LA modes and is defined by the precise dynamics of the kink formation and disappearance. The energy remaining in the LA modes after the buckling kink has relaxed continues to dissipate according to the mechanism characteristic of the first regime.

In addition to the energy drop at the onset of buckling, the maximum energy attained by the second radial mode in any given simulation is also a stochastic quantity. In particular, in simulations performed at the threshold conditions between the first and second regimes of stretching energy dissipation (initial temperature of 41 K and initial axial strain of 3.2%) and differing only in their instantaneous atomic positions and velocities at the time of the stretching deformation, the simulated trajectories took drastically different paths depending on whether the second radial mode energy reached the critical value and an axial buckling kink was formed (e.g., Fig. 8). Nevertheless, the probability of kink formation can be estimated as a function of the initial strain and temperature using the results of ten simulations performed for similar initial conditions [see Fig. 9(a)]. The probabilities at each initial temperature are fit with a logistic function. While the initial strain threshold for transition to stretching regime II increases with initial temperature, the excess energy of the second radial mode at which the transition occurs is essentially temperature independent.

The dependence of the mean waiting time required for the formation of a kink on the initial temperature and initial strain is shown in Fig. 9(b). This time corresponds to the duration
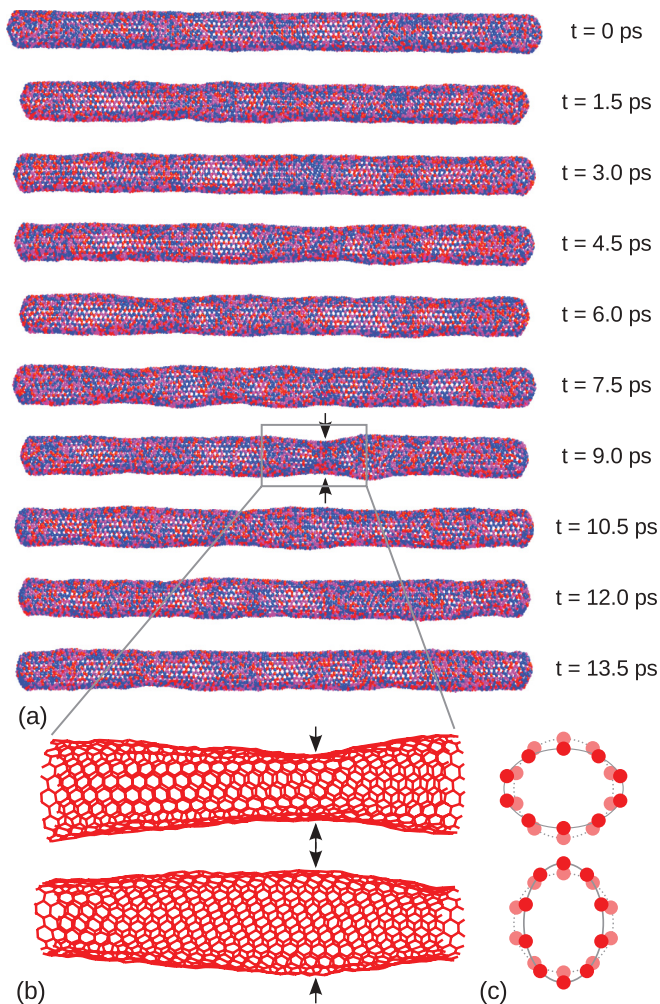
FIG. 7. (Color online) Snapshots of atomic configurations from a simulation performed with an initial temperature of 1054 K and an initial axial strain of 3.6% are shown in (a). As the length of the (10,10) CNT oscillates, the energy in the second radial mode increases (as can be seen from the ripples in the cross section) until an axial buckling kink is formed at about 9 ps (denoted by arrows). Atoms are colored according to their instantaneous kinetic energies, with red indicating higher energy. Enlarged views of two orthogonal projections of the segment of the CNT undergoing axial buckling are shown in (b). Schematic representations of CNT cross sections with atomic displacements corresponding to the second radial mode are shown in (c).

of the first step of the gradual energy dissipation in the three-step process of the stretching energy dissipation in the second regime, e.g., approximately 17 ps in Fig. 6(b). The waiting time is between 20 and 30 ps just above the threshold strain for the transition to the second stretching regime and decreases to approximately 1.5 ps as the initial strain is increased further.

The decrease in the waiting time to a duration comparable with the period of stretching oscillations signifies the transition to stretching regime III, in which an axial buckling kink forms within a single period of stretching oscillations, causing the immediate transfer of energy from the LA modes to other modes [see, e.g., Fig. 6(c)]. This transition occurs between initial strains of 4.2% and 5.8% for initial temperatures of 1054 and 41 K, respectively. The formation of the buckling kink

in this regime is caused by the collision of two compressive unloading waves propagating from the two ends of the initially stretched nanotube. The local compressive strain created by this collision, found to be at least 5% in all simulations in this third stretching regime, is sufficiently high to initiate axial buckling immediately.

The collision of the unloading waves, indicated by the regions of high local kinetic energy, and the resulting axial buckling kink formed between 1 and 1.5 ps after the beginning of the dynamic simulation can be seen in snapshots from simulations performed with an initial temperature of 568 K and an initial homogeneous axial strain of 6% (see Fig. 10) and an initial temperature of 1054 K and an initial strain of 10% (see Fig. 11). At an initial strain of 6%, the onset of axial buckling is first observed within an approximately 5-nm-wide central part of the nanotube (snapshots at 1.5 and 2 ps in Fig. 10). This is followed by the propagation of two buckling kinks away from the center of the CNT (snapshot at 2.5 ps in Fig. 10) and their eventual disappearance. The formation of the buckling kinks leads to a rapid dissipation of the energy of the excited LA modes, and the buckling kinks do not reappear in subsequent stretching oscillations. At a higher initial strain of 10%, the energy deposited in the CNT is sufficient to create multiple buckling kinks and large-scale distortions of the shape of the CNT (see Fig. 11). The deformation of the central part of the nanotube in this case is not limited to the axial shell buckling and involves a complex post-buckling behavior encompassing a combination of different buckling modes.

The minimum local compressive strain of 5% necessary for the immediate formation of an axial buckling kink in the third stretching regime agrees with the results of MD simulations performed under conditions of quasistatic compressive loading at relatively low temperatures, from zero to 100 K, in which the critical compressive strain for the onset of the axial shell buckling was found to be between 3.5 and 5.25% for (10,10) CNTs.[31,33–35] As in stretching regime II, the transfer of energy from the LA modes to other modes during the time of the buckling deformation is incomplete and continues via the slower mechanism characteristic of the first stretching regime once the axial buckling kink(s) has(have) relaxed.

While the general physical mechanisms responsible for transitions between different regimes of stretching energy dissipation can be expected to be independent of the length of the CNTs, the values of the initial strain corresponding to the transitions between the three regimes of stretching energy dissipation in a 26-nm-long (10,10) CNT cannot be directly applied to CNTs of different lengths. To explore the length dependence of the energy dissipation, we performed a series of simulations for CNTs with length ranging from 14 to 147 nm (50 to 600 unit cell rings) and the same values of initial temperature and axial strain, 568 K and 2%. The process of energy dissipation in the 50 unit cell CNT is essentially the same as in the 100 unit cell CNT discussed above (stretching regime I). The 200 unit cell CNT exhibits a reversible transfer of energy between the LA modes and the second radial mode [similar to Fig. 6(a)], indicative of the proximity to the transition to stretching regime II. The dissipation in the 400 and 600 unit cell CNTs is the three-step process typical of stretching regime II, with the waiting time for the onset of the axial buckling of about
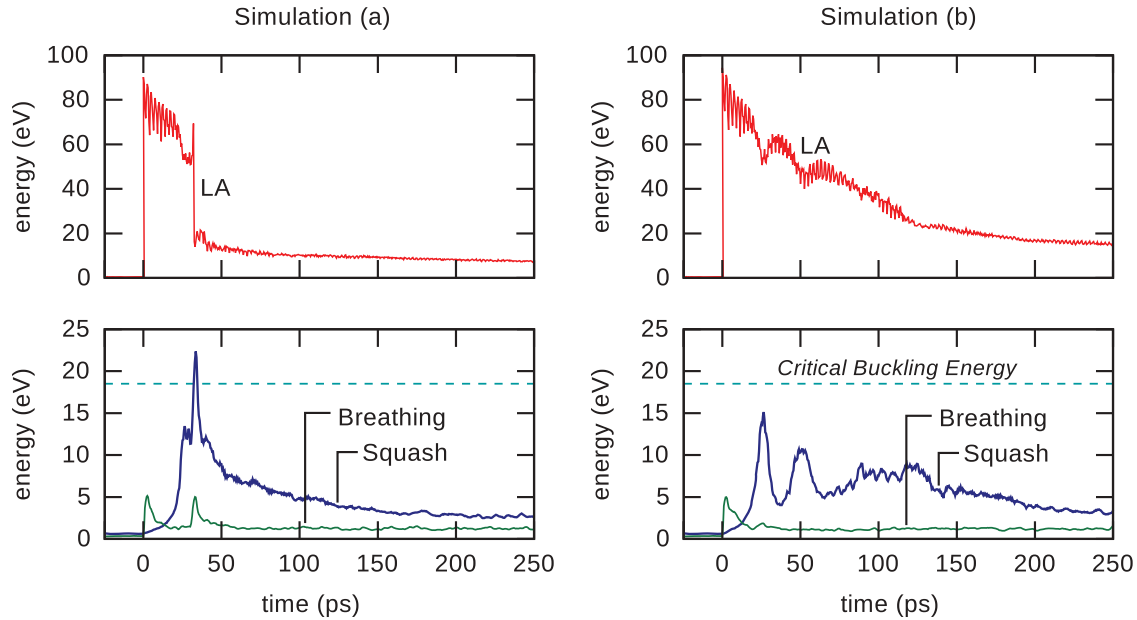
FIG. 8. (Color online) The evolution of the energy of the LA modes (top) and the second radial mode (bottom) in two simulations performed for the same initial temperature of 41 K and initial axial strain of 3.2%. The only difference between the two simulations is the instantaneous distribution of the atomic positions and velocities at the time of the stretching deformation. An axial buckling kink is formed at $t = 30$ ps in simulation *a* and is not observed in simulation *b*. The horizontal dashed line marks the critical value of the second radial mode energy required for the onset of axial buckling.

25 ps. The smaller initial strain required for the transition to stretching regime II can be explained by the local character of the axial buckling and the longer exposure of the central part of the CNT to compressive stresses generated by the interaction of the unloading waves propagating from the two ends of the nanotube. Thus both the total (length dependent) excess energy in the nanotube and the local transient concentration of the strain energy during the simulation (defined by the initial loading conditions) are additional factors affecting the mechanisms and rates of the energy dissipation.

C. Dissipation of BA mode vibrations

The analysis of the energy transfer from the BA modes is performed by following the evolution of the energies of all mode groups in free bending simulations in which equilibrated CNTs are instantaneously deformed (bent into an arc with a constant radius of curvature) at a time $t = 0$. Just as axial buckling is critical for defining the regimes of energy dissipation for stretching vibrations, bending buckling is found to play a prominent role in the energy dissipation of bending vibrations. Two distinct regimes of energy dissipation from the BA modes are established: slow temperature-dependent decay on the time scale of tens of nanoseconds in the absence of bending buckling (*bending regime I*), and fast temperature-independent energy transfer on the time scale of several periods of bending oscillations at levels of bending excitation sufficient for the formation of bending buckling kinks (*bending regime II*).

The energy relaxation in bending regime I is illustrated by a simulation performed at an initial temperature of 568 K and an initial radius of curvature of 30 nm [see Fig. 12(a)]. The drop of the energy of the BA modes from an initial value of 35 eV to

about 24 eV within the first picosecond, and the corresponding increase of the energies of the other modes, is related to the relaxation of the distortions of thermally fluctuating carbon-carbon bonds away from the neutral bending surface created by the instantaneous bending of the thermally equilibrated CNT. As a result, not all of the initial bending energy is deposited into the BA modes. The subsequent evolution of the energy of the BA modes exhibits a very slow dissipation of the energy of the bending vibrations that is barely visible on the time scale of 250 ps shown in Fig. 12; the half-life of the bending excitation defined with respect to the energy of the BA modes after the initial drop is estimated to be 26 ns in this simulation. The slow rate of decay of the bending energy is consistent with the results of earlier simulations of free bending vibrations of a shorter 10-nm-long (10,10) CNT in which no measurable decrease in the amplitude of oscillations was detected over hundreds of vibrational periods.[24] No anomalously fast dissipation of bending oscillations similar to that reported in Ref. 25 is observed in the simulations performed in the first regime with initial temperatures up to 1054 K, suggesting that the anomalous dissipation is likely to be specific to the double clamping of the CNTs imposed by the periodic boundary conditions used in Ref. 25. The double clamping may facilitate coupling of the bending vibrations to the LA modes that have much faster dissipation rates (see Sec. II B).

The energy dissipation in bending regime II is illustrated in Fig. 12(b), in which fast thermalization of the energy of bending vibrations is observed during the first 50 ps after the initial drop of the buckling energy. In this simulation, which was performed at an initial temperature of 568 K and an initial radius of curvature of 15 nm, the amplitude of bending oscillations is high enough to create buckling kinks at every half period of the first two bending oscillations. For a similar
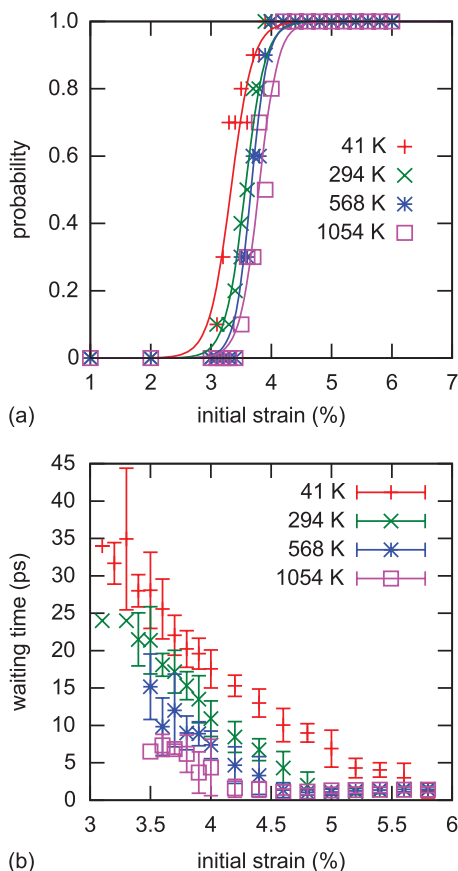
(a)

(b)

FIG. 9. (Color online) The probability of the formation of an axial buckling kink and observing the immediate dissipation of the LA energy (a) and the mean waiting time until this event occurs (b). Shown with the probabilities are the best fits of logistic regressions for each initial temperature. The transition to the third regime is defined where the mean waiting time drops to less than one period of stretching oscillation (less than 3 ps); this transition occurs between 4.2% and 5.8% initial strain for initial temperatures 1054 and 41 K, respectively. Error bars are not shown in (b) for strains at which the formation of a kink was observed in only one simulation.

simulation performed at a higher temperature of 1054 K, the snapshots shown in Fig. 13 for the first half period of the first bending oscillation after the initial deformation provide a visual picture of the transient formation of the buckling kinks. The energy of the BA modes drops from 88 eV to about 60 eV within the first picosecond, and the CNT quickly relaxes from its semicircular profile to form two bending buckling kinks. The buckling kinks shift towards each other, merge at about 4.5 ps, and disappear as the CNT straightens up by about 7 ps. The buckling points reappear during the following 3 cycles of bending oscillations but cease to exist by $t = 50$ ps. Once the energy of the BA modes decreases below the minimum required for the formation of the buckling kinks, the dissipation rate drops dramatically, and thermalization continues through the mechanism characteristic of bending regime I. The observation of fast energy dissipation in the regime in which the CNT experiences bending buckling is consistent with the fast energy dissipation reported for a (5,5) cantilevered CNT that was highly deformed and buckled in its initial state.[23]
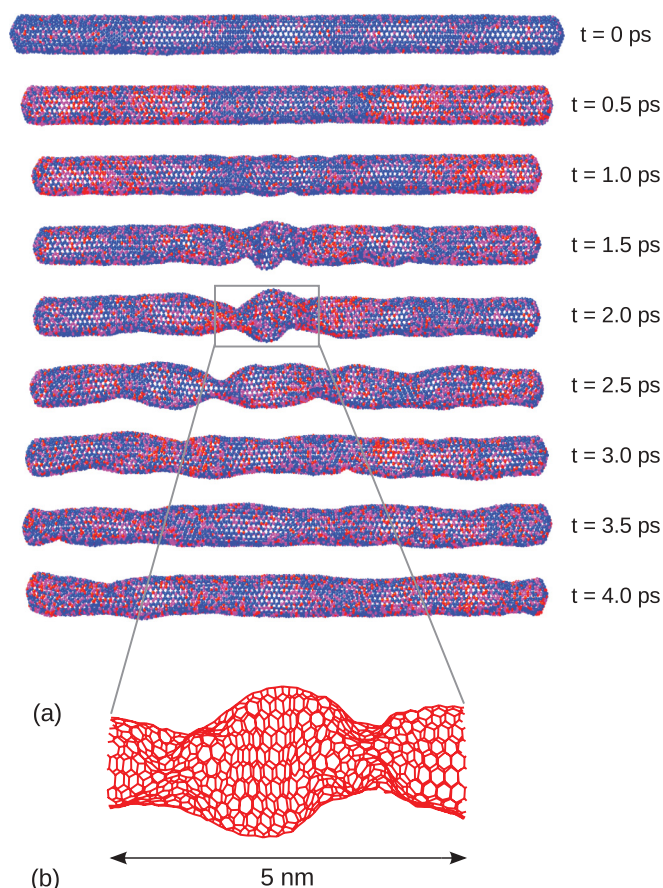

(a)

(b)

FIG. 10. (Color online) Snapshots of atomic configurations from a simulation of a CNT with an initial temperature of 568 K and an initial homogeneous axial strain of 6% are shown in (a). Atoms are colored according to their instantaneous kinetic energies, with red indicating higher energy. An enlarged view of a segment of the CNT undergoing axial buckling at a time of 2 ps is shown in (b).

The results of the calculation of the decay rates obtained in the dynamic bending simulations performed for four initial temperatures, 41, 294, 568, and 1054 K, and seven values of the initial radius of curvature, 10, 15, 25, 30, 50, 75, 100, and 1000 nm, are shown in Fig. 14. As in the analysis of the stretching vibrations, the rate of the bending energy dissipation is evaluated as a function of the instantaneous temperature θ of the HB modes and the instantaneous excess energy in the BA modes above the equilibrium value E_{BA}^{θ} that corresponds to the instantaneous temperature θ, $E_{BA}^{\theta} = 198 k_B \theta$. Each simulation produces a range of decay rates corresponding to the variation of the excess energy in the BA modes, $E_{BA} - E_{BA}^{\theta}$, and the temperature θ along the simulated trajectories.

There is a sharp increase in the energy decay rate by more than an order of magnitude once the excess energy in the BA modes reaches the critical value E_{BA}^* required for the dynamic buckling kink formation [see Fig. 14(a)]. This threshold behavior allows us to draw a clear distinction between the two regimes of bending energy dissipation that have drastically different dissipation rates and dependences on the excess bending energy. An enlarged view of the dependence of the decay rates on the excess energy in bending regime I is shown in Fig. 14(b). These decay rates are about
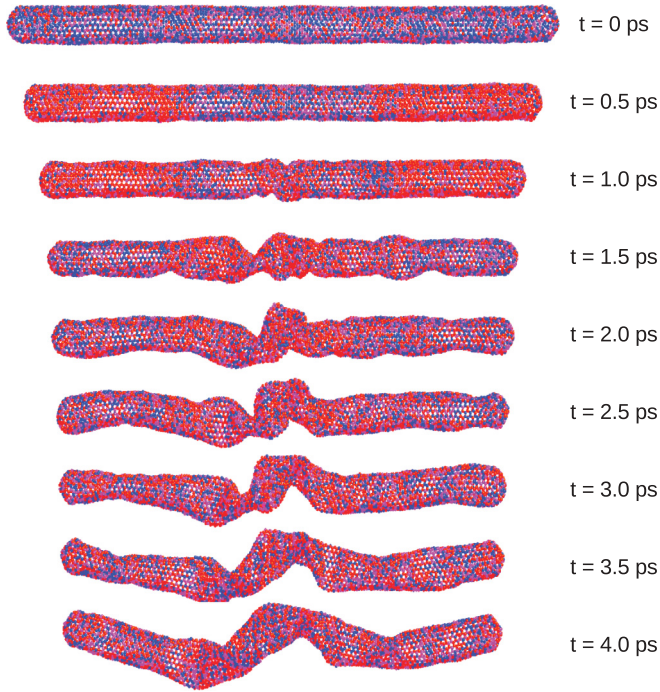
FIG. 11. (Color online) Snapshots of atomic configurations from a simulation of a CNT with an initial temperature of 1054 K and an initial homogeneous axial strain of 10%. Atoms are colored according to their instantaneous kinetic energies, with red indicating higher energy.

two orders of magnitude lower than those of the first LA dissipation mechanism. Within the calculation error, the decay rate in bending regime II can be considered to be temperature independent [see Fig. 14(a)].

The functional dependence of the decay rate on the relative excess energy $(E_{BA} - E_{BA}^{\theta})/E_{BA}^{\theta}$ and the equilibrium energy E_{BA}^{θ} used as a proxy for the temperature can be written in a form applicable to both the first and second regimes of bending energy dissipation:

$$
\begin{aligned}
\frac{d}{dt}&\left(E_{BA} - E_{BA}^{\theta}\right) \\
&= -\gamma^{BA(I)} \left(\frac{E_{BA} - E_{BA}^{\theta}}{E_{BA}^{\theta}}\right)^{\alpha^{BA(I)}} \left(E_{BA}^{\theta}\right)^{\beta^{BA(I)}} \\
&\quad - \gamma^{BA(II)} \left(\frac{E_{BA} - E_{BA}^{\theta}}{E_{BA}^{\theta}}\right)^{\alpha^{BA(II)}} \left(E_{BA}^{\theta}\right)^{\beta^{BA(II)}} \\
&\quad \times H\left[\left(E_{BA} - E_{BA}^{\theta}\right) - E_{BA}^{*}\right], \tag{13}
\end{aligned}
$$

where $H(E)$ is the Heaviside step function, the critical excess energy for the onset of buckling $E_{BA}^{*} = 13.5$ eV is estimated from the data shown in Fig. 14(a), and the best fits for the adjustable parameters are

$$\gamma^{BA(I)} = (4.58 \pm 0.58) \times 10^{-4} \, (\text{eV}^{1-\beta^{BA(I)}} \text{ps}^{-1}),$$

$$\alpha^{BA(I)} = 1.01 \pm 0.07, \quad \beta^{BA(I)} = 1.44 \pm 0.06,$$

$$\gamma^{BA(II)} = (4.49 \pm 0.81) \times 10^{-2} \, (\text{eV}^{1-\beta^{BA(II)}} \text{ps}^{-1}),$$

$$\alpha^{BA(II)} = 0.94 \pm 0.07, \quad \beta^{BA(II)} = 0.84 \pm 0.06.$$

As can be seen from Fig. 14, this set of parameters provides a good description of the data points for both regimes of energy dissipation. In both regimes, the decay of the energy of bending oscillations appears to be exponential since both $\alpha^{BA(I)}$ and $\alpha^{BA(II)}$ equal unity within the calculated error. The fact that the values of $\alpha^{BA(II)}$ and $\beta^{BA(II)}$ are similar reflects the lack of temperature dependence of the decay rate in bending regime II. The mechanisms responsible for energy dissipation in bending regime I are likely to be at work in the second regime as well, albeit with a negligible contribution to the total rate of dissipation. It is therefore not necessary to switch off the contribution of the slow dissipation characteristic of the first regime when considering energy dissipation in bending regime II.

III. DISSIPATION OF ACOUSTIC VIBRATIONS IN THE MESOSCOPIC MODEL OF CNTs

The results of the atomistic simulations described above provide a general framework for designing a computational description of acoustic energy dissipation in the mesoscopic model of CNTs, which does not include an explicit representation of the radial and HB vibrational modes. While there are still some uncertainties with respect to the effects of the initial loading conditions (e.g., excitation of an acoustic pulse rather than homogeneous straining of CNTs or simultaneous excitation of different groups of vibrational modes) and the parameters of the nanotubes (e.g., length, diameter, chirality, or multi- versus single-walled type), the conditions established in the MD simulations for transitioning between distinct physical regimes of energy dissipation and the characteristic time scales of energy dissipation in the different regimes provide a solid foundation for designing a computational description of energy dissipation in the mesoscopic model. In this section, an outline of the main principles of the mesoscopic model is followed by a description of the computational approach designed to account for the energy exchange between the dynamic degrees of freedom of the mesoscopic model and the internal thermal energy of nanotubes. The enhanced mesoscopic model is then tested by reproducing the energy dissipation in free vibrations of individual CNTs predicted in the atomistic simulations.

A. Mesoscopic dynamic model of nanotubes

The mesoscopic model[7,8,11] for simulation of CNT-based materials and nanocomposites adopts a coarse-grained description of nanocomposite constituents (CNTs and matrix molecules), with individual CNTs represented as chains of stretchable cylindrical segments. Each CNT is defined by the positions of nodes joining neighboring segments, and the dynamics of a system of interacting CNTs are determined by solving the equations of motion of classical mechanics for the positions of all nodes. The forces acting on the nodes are calculated based on the mesoscopic force field that accounts for the internal stretching, bending and buckling of nanotubes, as well as the van der Waals interactions among the CNTs. The harmonic parts of the stretching and bending potentials are described by Eqs. (1) and (2) and are parameterized[7] for single-walled CNTs based on the results of atomistic simulations performed with the reactive empirical bond-order (REBO) potential.[36] The transition to the anharmonic regime
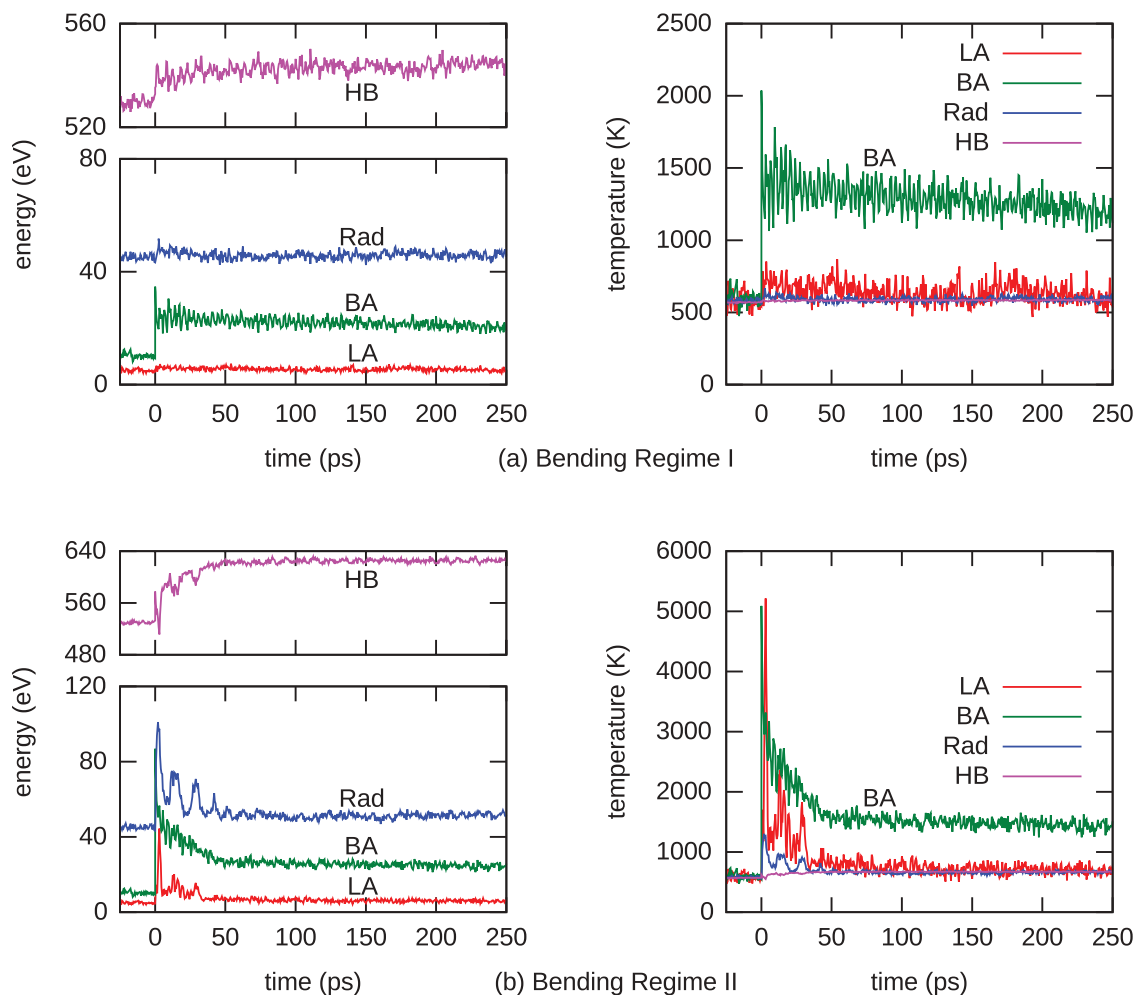
FIG. 12. (Color online) The evolution of the energies of the LA, BA, Rad, and HB modes in simulations performed for CNTs equilibrated at a temperature of 568 K and bent into an arc with a constant radius of curvature equal to 30 nm (a) and 15 nm (b) at time $t = 0$. In the right panels, the values of energy are converted to temperature units for each group of modes by dividing the energy values by the product of the corresponding number of modes present in each group and the Boltzmann constant. The periodic formation of a bending buckling kink in (b) is reflected in the large oscillations in the stretching and radial energies observed until approximately 50 ps as well as in the faster decay of the bending energy during this time.

(nonlinear stress-strain dependence), fracture of CNTs under tension and bending as well as bending and axial shell buckling behavior are accounted for in the model.

The mesoscopic description of bending buckling is provided in Ref. 11. The bending buckling is assumed to occur at mesoscopic nodes of CNTs where the local radius of curvature R_{bnd}^{bcl} reaches a critical value of 27.5 nm, chosen to be within the range of values predicted in quasistatic atomistic MD simulations of (10,10) CNTs.[30,31] In the postbuckling state, the bending potential includes an additional term that is proportional to the buckling angle and accounts for the strain energy in a small vicinity of the buckling point. The parameterization of the bending buckling potential ensures that the drop in the slope of the bending energy dependence on the bending angle upon buckling is in quantitative agreement with the results of atomistic simulations performed for various single-walled CNTs.[11]

The axial shell buckling is assumed to occur in mesoscopic segments where the compressive strain exceeds $|\varepsilon_{str}^{bcl}| = 0.04$.

This value of critical strain is within the range of values predicted for (10,10) CNTs in quasistatic atomistic MD simulations, e.g., 0.035 for 9.6-nm-long CNTs in Ref. 35, 0.04 for 10-nm-long CNTs in Ref. 34, and 0.0525 for 7-nm-long CNTs in Ref. 33. The axial buckling results in a transition from the quadratic to linear dependences of the strain energy on the axial strain and an abrupt drop in the axial stress. In the mesoscopic model, the axial buckling in a segment defined by nodes i and $i + 1$ is represented by replacing the corresponding quadratic term in the sum over all of the mesoscopic segments in Eq. (1) with a linear term, $k_{str}^{bcl} a |\varepsilon_{str}^{i,i+1}|$, where $\varepsilon_{str}^{i,i+1} = (|\vec{r}^{i+1} - \vec{r}^i| - a)/a$. The value of k_{str}^{bcl} is chosen to satisfy an approximate relation, $k_{str} |\varepsilon_{str}^{bcl}|/k_{str}^{bcl} = 2.8$. This relation is based on the results of atomistic simulations, in which the axial stress of a (10,10) CNT is observed to drop upon axial shell buckling by a factor of 2.7 in Ref. 34 and by a factor of 2.9 in Ref. 35. In order to limit the maximum value of the compressive strain and to allow the buckling region to extend beyond one mesoscopic segment, this regime of
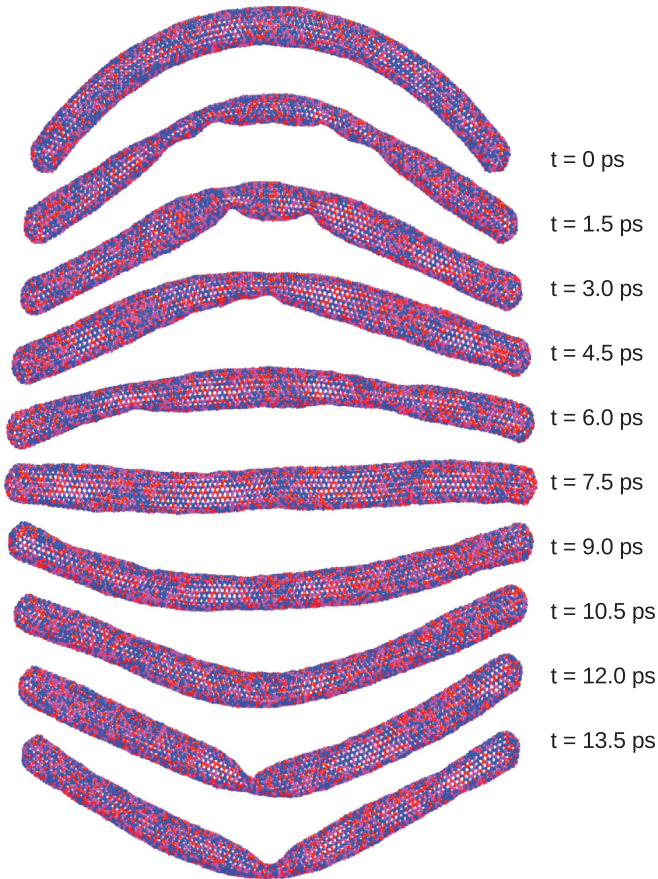
FIG. 13. (Color online) Snapshots of atomic configurations in a simulation of free bending vibrations with an initial temperature of 1054 K and an initial radius of curvature of 15 nm (bending regime II). The snapshots are shown for the first half period of the first bending oscillation after the initial deformation. Atoms are colored according to their instantaneous kinetic energies, with red indicating higher energy.

constant axial stress reverts to the quadratic regime with the same k_{str} used at small strains when the axial strain reaches $\varepsilon_{str}^{bcl-max}$ [see Fig. 15(a)]. The value of $|\varepsilon_{str}^{bcl-max}|$ controls the size of the buckling region in the third regime of stretching oscillations (see Sec. II B) and is chosen to be 0.45 to match the approximate size of the buckling region, about 5 nm, in the simulation performed for an initial axial strain of 6% and an initial temperature of 568 K (see Fig. 10).

The intertube interactions are calculated based on the tubular potential method[8,37] that allows for a computationally efficient and accurate representation of van der Waals interactions between CNT segments of arbitrary lengths and orientation. The tubular potential is parameterized to match the atomistic representation of the intertube interactions (summation over pairs of interacting carbon atoms) as described within the AIREBO potential.[28] Since the coupling of low-frequency modes among different CNTs via van der Waals interactions is explicitly represented in the mesoscopic model and since there is a relatively slow energy exchange between the low and high frequency vibrational modes within the CNTs, the implementation of the acoustic energy dissipation in individual CNTs, described in the next section, can be expected to ensure
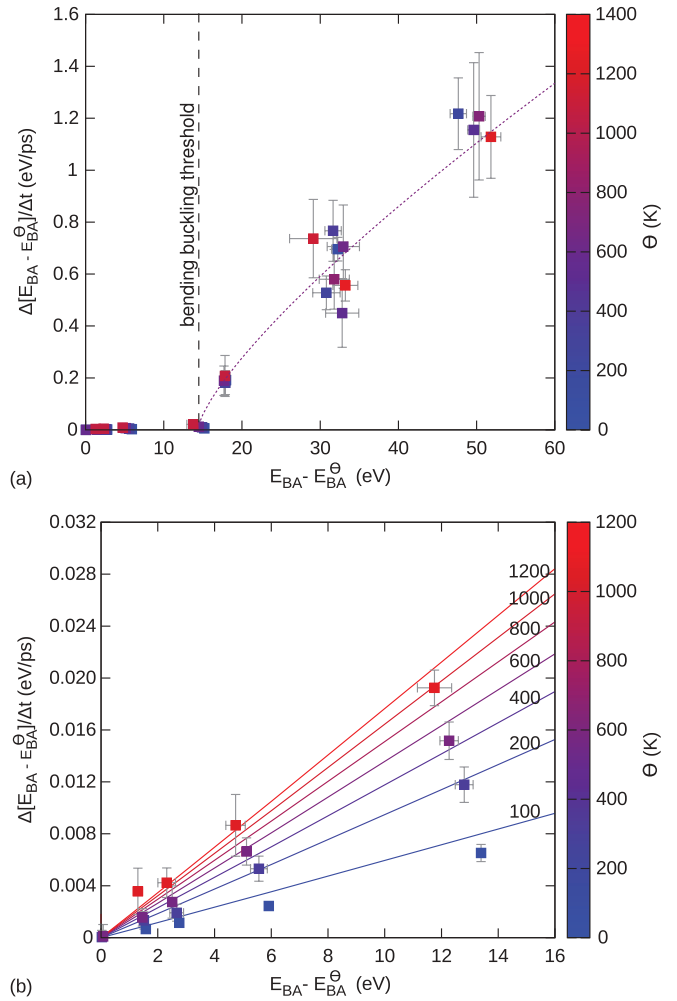

FIG. 14. (Color online) The rate of energy dissipation from the excited BA modes as a function of the excess BA energy for all initial radii of curvature (a) and for initial radii of curvature greater than the critical value for dynamically forming a bending buckling kink, approximately 27 nm (b). The vertical dashed line in (a) marks the critical value of the excess bending energy E_{BA}^* corresponding to the onset of bending buckling and the transition from the first to the second regime of bending energy dissipation. The data points are obtained by averaging over ten simulations performed for each combination of initial bending strain and initial temperature. Isothermal contours of the fitted function given by Eq. (13) are shown in (b) for temperatures ranging from 100 to 1200 K. The temperature-independent fit to the buckling decay rates is shown by a dashed line in (a).

an adequate representation of the thermalization of mechanical energy in CNT materials.

In order to facilitate comparison between the results of mesoscopic and atomistic simulations, the equilibrium length of CNT segments, 2.6 Å, is chosen in this work to ensure that the number of longitudinal and bending modes in the mesoscopic model matches the number of CNT unit cells in the atomistic representation of the CNT discussed in Sec. II. The corresponding energies associated with these groups of modes can then be directly related to the predictions of the atomistic simulations. In practical applications of the mesoscopic model,[7,8,11–13] however, the equilibrium length

of CNT segments is typically much longer and can exceed the length of the unit cell by an order of magnitude. As briefly discussed in Sec. II A, the use of the longer segments in the mesoscopic representation of CNTs introduces artificial cutoff frequencies for LA and BA modes and reduces the number of acoustic modes that are explicitly represented in the mesoscopic model. The acoustic modes eliminated by the coarse graining of the mesoscopic model are joined with the HB group of modes and are represented by internal heat bath variables as discussed below.

B. Heat bath approach for mesoscopic description of energy dissipation

The computational approach developed here for the description of the thermal properties of CNTs in the mesoscopic model is based on the introduction of "heat bath" variables representing the energy content of the vibrational modes that are not explicitly represented in the coarse-grained mesoscopic model. The heat bath variables can be associated with each dynamic element of the model (segment of a CNT) or with the entire CNT. The latter option is used in the heat bath approach implemented in this work. While the implementation of local heat baths associated with CNT segments does not present technical difficulties, the high values of the intrinsic thermal conductivity of CNTs, predicted in atomistic simulations[38,39] and confirmed experimentally,[40,41] and the nonlocal nature of the low-frequency acoustic modes suggest that long-term spatial localization of thermal energy in a part of a nanotube is unlikely.

The heat capacity of the bath can be obtained either by subtracting the contribution of the dynamic degrees of freedom from the experimental specific heat of CNTs[26,27] or by evaluating its theoretical value based on the equipartition and virial theorems of classical mechanics. The latter approach allows for the direct quantitative comparison with the results of classical atomistic MD simulations and is used in the test simulations presented in Sec. III C. The exchange of energy between the internal heat bath and the dynamic degrees of freedom of the mesoscopic model is designed such that the rates of energy dissipation established in the atomistic simulations (see Secs. II B and II C) are reproduced in the mesoscopic simulations. The results of the atomistic simulations suggest that the occurrence of axial or bending buckling results in the rapid thermalization of the energy of acoustic vibrations on a time scale comparable to several periods of stretching or bending oscillations. The dissipation of weakly excited acoustic vibrations at the initial strains that do not lead to the buckling, on the other hand, is much slower and takes place on time scales of hundreds of picoseconds for stretching vibrations and tens of nanoseconds for bending vibrations. The large disparity between the dissipation rates with and without buckling necessitates the development of two complementary methods for describing energy dissipation in the mesoscopic model.

The slow dissipation of the acoustic vibrations is modeled by introducing damping forces into the equations of motion in the mesoscopic model. Due to the large disparity between the decay rates predicted in the atomistic simulations for stretching and bending vibrations, it is necessary to apply different damping forces for the bending and stretching motions of the nanotube. To achieve this, the "thermal" velocity of each node $\vec{v}^i$ (calculated by removing the contributions from the total linear and angular momenta of the CNT) is decomposed into stretching and bending components that are parallel and perpendicular to the local direction of the elastic line of the CNT, respectively. The velocity components of node i are calculated as $\vec{v}^i_{str} = (\vec{v}^i \cdot \vec{e}^i)\vec{e}^i$ and $\vec{v}^i_{bnd} = \vec{v}^i - \vec{v}^i_{str}$. The damping force acting on node i is then defined as a sum of two terms affecting the bending and stretching energy of the nanotube:

$$\vec{F}^i_d = -\xi_{str} m^i \vec{v}^i_{str} - \xi_{bnd} m^i \vec{v}^i_{bnd}, \quad (14)$$

where m^i is the mass of a part of the nanotube represented by the node i and the damping coefficients ξ_{str} and ξ_{bnd} are chosen to match the energy dissipation rates predicted in the atomistic simulations, as discussed below. The damping forces are added to the forces acting on the node due to the mesoscopic force field discussed in Sec. III A, and the total forces are used in the integration of the equations of motion of the nodes. Note that the addition of the damping forces defined by Eq. (14) may violate conservation of the angular and linear momenta of the nanotube. To correct for this, the contributions of the damping forces to the net force and torque acting on the CNT are calculated and subtracted out. The damping forces are then renormalized in order to achieve the desired energy transfer rate.

The energies of stretching and bending vibrations in the mesoscopic model, E_{str} and E_{bnd}, are calculated as a sum of potential and kinetic energy terms associated with each type of motion. Since in the test simulations performed in this work the equilibrium length of the mesoscopic segments is equal to the length of a CNT unit cell, the energy terms are defined analogously to the energies of the LA and BA modes in the analysis of the atomistic results, Eqs. (1)–(4). For a given temperature θ of the heat bath modes, the instantaneous decay rates for the stretching and bending energies are defined by Eqs. (12) and (13). Given that the LA and BA modes represent a small fraction of all vibrational modes in the CNT, the increase of E^θ_{LA} and E^θ_{BA} due to the dissipation of the stretching and bending vibrations (and the corresponding increase of the heat bath temperature θ) can be expected to be much slower than the decay of the excited LA or BA modes. Therefore, in order to simplify the implementation of the heat bath in the mesoscopic model, the time derivatives of E^θ_{LA} and E^θ_{BA} in Eqs. (12) and (13) are neglected, and the dissipation of the stretching and bending energy is described as

$$\frac{dE_{str}}{dt} \cong \frac{d(E_{LA} - E^\theta_{LA})}{dt} \text{ and } \frac{dE_{bnd}}{dt} \cong \frac{d(E_{BA} - E^\theta_{BA})}{dt}. \quad (15)$$

The amounts of energy transferred between the stretching and bending vibrations and the heat bath modes during a time step Δt of a dynamic mesoscopic simulation can then be expressed as

$$\Delta E_{str} = \frac{d(E_{LA} - E^\theta_{LA})}{dt}\Delta t \text{ and } \Delta E_{bnd} = \frac{d(E_{BA} - E^\theta_{BA})}{dt}\Delta t. \quad (16)$$
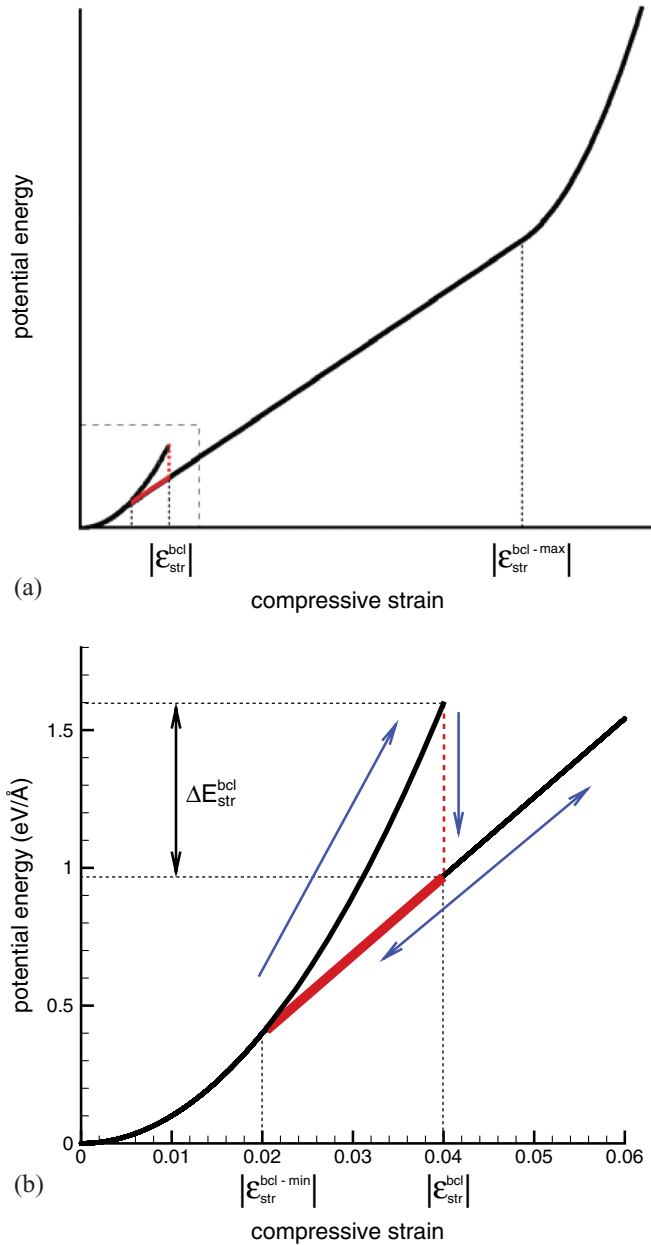
(a)

(b)

FIG. 15. (Color online) An illustration of the hysteresis approach to the localized energy dissipation upon buckling in the mesoscopic model. The compressive part of the axial strain energy is shown schematically in (a), and an enlarged view of the hysteresis region is shown in (b). The blue arrows in (b) represent the path followed when a buckling kink is created. The red segments of the plot are the irreversible parts of the strain energy hysteresis. $\Delta E_{\mathrm{str}}^{\mathrm{bcl}}$ is the amount of energy transferred to the heat bath of the CNT in each buckling cycle.

To carry out the energy transfer, the coefficients ξ_{str} and ξ_{bnd} in Eq. (14) are defined according to an expression derived in Ref. 16:

$$\xi_{\mathrm{str}} = \frac{\Delta E_{\mathrm{str}}}{\Delta t \sum_{i=1}^{N} m^i \left(\vec{v}_{\mathrm{str}}^{\,i}\right)^2} \text{ and } \xi_{\mathrm{bnd}} = \frac{\Delta E_{\mathrm{bnd}}}{\Delta t \sum_{i=1}^{N} m^i \left(\vec{v}_{\mathrm{bnd}}^{\,i}\right)^2}. \tag{17}$$

The coefficients calculated from these equations ensure that the energy removed from the bending and stretching motions due to the action of the damping forces is equal to $\Delta E_{\mathrm{str}} + \Delta E_{\mathrm{bnd}}$. This energy is then deposited into the heat bath, leading to the heat bath temperature increase, $\theta(t + \Delta t) = \theta(t) + \Delta\theta$, where

$$\Delta\theta = \frac{1}{c_{\mathrm{HB}}}(\Delta E_{\mathrm{str}} + \Delta E_{\mathrm{bnd}}) \tag{18}$$

and c_{HB} is the heat capacity associated with the heat bath modes. As discussed above, the theoretical value of the heat capacity, evaluated by neglecting quantum and anharmonic effects, is used in the calculations performed in this work. For a CNT composed of n_{at} atoms and represented in the mesoscopic model by N nodes, $c_{\mathrm{HB}} = 3(n_{\mathrm{at}} - N)k_B$.

The sharp increase in the energy dissipation rates at the onset of buckling is accounted for by adding another dissipation mechanism involving fast, localized thermalization in the vicinity of buckling kinks. This mechanism is necessary because the damping forces are applied globally and remove energy from all nodes of the nanotube, whereas buckling occurs locally and results in energy dissipation predominantly in the vicinity of a buckling kink. A number of initial test simulations demonstrate that increasing the magnitude of the damping forces (in order to match the sharp increase in the rate of energy dissipation upon buckling) results in the preferential energy removal from nodes that have high velocities, which are generally not the buckled nodes. As a result, strong damping results in the persistence of buckling kinks for an unrealistically large number of periods of oscillation.

In order to overcome this shortcoming, a complementary approach based on the introduction of hysteresis loops in the potentials describing the bending and stretching energy of the segments experiencing buckling deformation is developed. This hysteresis approach is illustrated in Fig. 15, where the compressive part of the axial strain energy is shown for a range of strains including both $\varepsilon_{\mathrm{str}}^{\mathrm{bcl}}$ and $\varepsilon_{\mathrm{str}}^{\mathrm{bcl-max}}$ in Fig. 15(a), and an enlarged view of the hysteresis region is shown in Fig. 15(b). A similar hysteresis loop is also introduced in the potential describing the dependence of the bending strain energy on the local radius of curvature. The potential remains harmonic up to the critical buckling strain $|\varepsilon_{\mathrm{str}}^{\mathrm{bcl}}|$ and switches to a linear dependence on the compressive strain in the buckling region [black curve in Fig. 15(b)]. To enable the localized energy dissipation, a hysteresis loop is introduced in the potential by extending the linear regime to axial strains below the threshold for buckling [red solid line in Fig. 15(b)]. The transition to the linear regime takes place at a strain $\varepsilon_{\mathrm{str}}^{\mathrm{bcl}}$, where the strain energy experiences a drop by $\Delta E_{\mathrm{str}}^{\mathrm{bcl}}$ [red dashed line in Fig. 15(b)]. After unbuckling takes place at $\varepsilon_{\mathrm{str}}^{\mathrm{bcl-min}}$, the energy follows the original form of the potential (black line in Fig. 15) until the next buckling takes place at $\varepsilon_{\mathrm{str}}^{\mathrm{bcl}}$. In each buckling-unbuckling cycle, the energy $\Delta E_{\mathrm{str}}^{\mathrm{bcl}}$ is removed from the dynamic simulation and transferred into the heat bath (i.e., the heat bath temperature increases by $\Delta\theta = \Delta E_{\mathrm{str}}^{\mathrm{bcl}}/c_{\mathrm{HB}}$). The value of $\Delta E_{\mathrm{str}}^{\mathrm{bcl}}$ and, therefore, the rate of the localized stretching energy dissipation in the buckling regime are controlled by the choice of $\varepsilon_{\mathrm{str}}^{\mathrm{bcl-min}}$ and can be chosen to match the predictions of the atomistic simulations. The value of $\Delta E_{\mathrm{str}}^{\mathrm{bcl}}$ is maximized when $\varepsilon_{\mathrm{str}}^{\mathrm{bcl-min}}$ is chosen
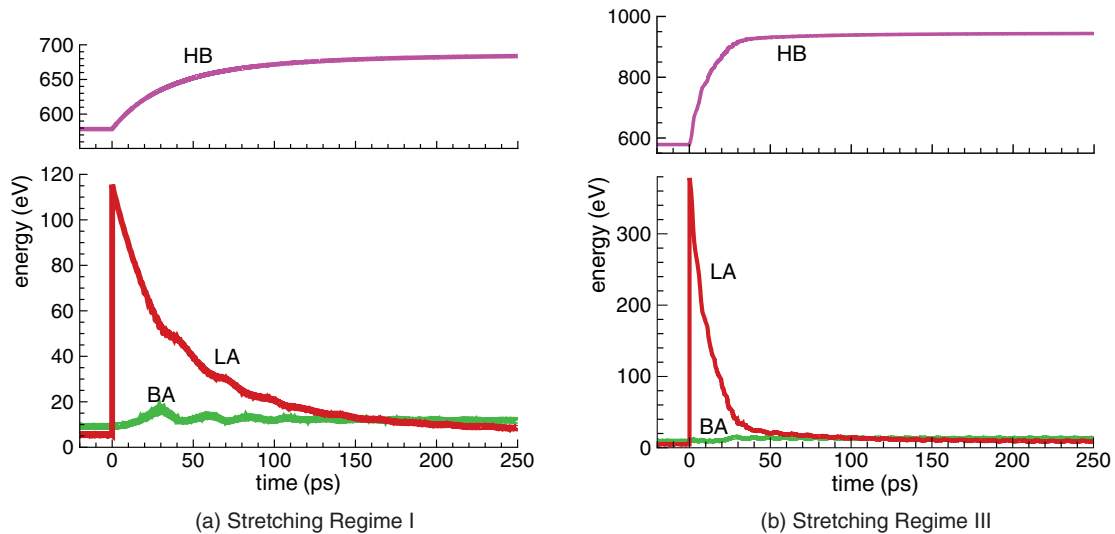
FIG. 16. (Color online) The evolution of the energies of the LA, BA, and HB modes in mesoscopic simulations performed for CNTs equilibrated at a temperature of 568 K and homogeneously stretched at time $t = 0$ with initial axial strains of 3% (a) and 6% (b). The analogous plots for the atomistic simulations are shown in Figs. 3(a) and 3(c). In contrast to the atomistic simulations, the Rad modes are included within the HB modes in the mesoscopic simulations.

such that the slopes of the quadratic and the linear portions of the potential are equal at $\varepsilon_{\text{str}}^{\text{bcl}-\text{min}}$ [this is not the case in Fig. 15(b), where $|\varepsilon_{\text{str}}^{\text{bcl}-\text{min}}| = 0.02$ is used in the plot, and the maximum dissipation is achieved at $|\varepsilon_{\text{str}}^{\text{bcl}-\text{min}}| = 0.0142$]. The choice of $\varepsilon_{\text{str}}^{\text{bcl}-\text{max}}$ also affects the rate of energy dissipation, as the number of buckling kinks in the buckling region of a CNT increases with decreasing $|\varepsilon_{\text{str}}^{\text{bcl}-\text{max}}|$. The implementation of the hysteresis approach to the energy dissipation in bending buckling is similar to the one described above for the axial compression. The analogous parameters controlling the energy dissipation in this case are the unbuckling radius of curvature $R_{\text{bnd}}^{\text{bcl}-\text{min}}$ and the corresponding energy drop $\Delta E_{\text{bnd}}^{\text{bcl}}$.

The strain energy hysteresis illustrated in Fig. 15 is similar to the hysteresis loop observed in strain energy curves predicted in quasistatic MD simulations of bending buckling,[30,42] where the difference between the loading and unloading curves is attributed to the van der Waals attraction between the collapsed walls at the kinked site. In the mesoscopic model, however, hysteresis is not intended to reproduce the real evolution of the strain energy during the formation and disappearance of the buckling kinks. Rather, the energy hysteresis in the mesoscopic model is used as a mechanism for transferring energy from the acoustic vibrations to the nanotube heat bath. This hysteresis approach, in which the energy of bending and stretching vibrations is removed locally at the buckling kinks in pre-defined amounts, yields better agreement with the results of the atomistic simulations as compared to an approach in which only frictional dissipation is applied by means of damping forces.

In simulations of CNT materials, it is possible to distinguish between dynamic buckling (when the energy of acoustic vibrations should be dissipated) and quasi-static buckling in the course of slow deformation (when the potential energy should follow the original path on the strain energy curve and not experience hysteresis). Consideration of the latter case is not a concern in the dynamic simulations presented below, and

thus no modifications to the model have been made to account for it. In cases in which quasistatic buckling is important, however, it would be possible to associate a "clock" with each buckling event, and the time in the buckled state could be monitored for each node that experiences buckling. Hysteresis would only be invoked when the time in the buckled state is less than predefined values of $t_{\text{str}}^{\text{bcl}-\text{max}}$ and $t_{\text{bnd}}^{\text{bcl}-\text{max}}$, chosen to be larger than periods of stretching and bending oscillations, respectively. If a buckling kink should persist for a longer time, then unbuckling would proceed through the original path on the strain energy curve, and no energy transfer to the heat bath would occur.

Note that in systems composed of multiple interacting CNTs (such as CNT films, mats, or buckypaper), the interaction among the nanotubes can be expected to facilitate coupling among vibrational modes and to substantially reduce the time required to dissipate the mechanical energy in the absence of buckling. With the introduction of the heat bath and the two mechanisms of energy dissipation discussed above, the mesoscopic model can be expected to provide a more accurate representation of fast dynamic phenomena, such as the projectile impact illustrated in Fig. 1, in which strong deviations from thermal equilibrium are expected for different groups of vibrational modes.

C. Energy dissipation in mesoscopic modeling of free vibrations of CNTs

A series of mesoscopic simulations of free vibrations of individual CNTs were performed to test the ability of the heat bath approach to reproduce the energy dissipation predicted in the atomistic simulations. Free bending and stretching simulations were performed for a range of initial strains covering the different dissipation regimes identified in Secs. II B and II C.

The energy dissipation in the two stretching regimes, below and above the threshold for axial buckling (stretching

regimes I and III, respectively) are illustrated in Fig. 16, where the evolution of stretching, bending, and heat bath energies is shown for mesoscopic simulations performed with an initial temperature of 568 K and two values of initial strain, 3% and 6%. At an initial strain of 3%, the decay rate of the stretching energy closely follows the prediction of Eq. (12). The plots in Fig. 16(a) can be directly related to the corresponding plots in Fig. 3(a) obtained in an atomistic simulation performed for the same initial strain. The plots are in good agreement, with the exception of several minor quantitative differences. The somewhat higher initial stretching energy in the mesoscopic simulation can be explained by the difference in the interatomic potentials used in the parameterization of the mesoscopic model (REBO)[7,36] and in the atomistic simulations performed in this work (AIREBO)[28] as well as by the method used for the stretching excitation in the atomistic simulations (instantaneous scaling of atomic positions in the equilibrated CNT reduces the thermal component of the stretching energy at the beginning of the simulation). The heat bath in the mesoscopic model includes the radial modes which are considered separately in the analysis of atomistic simulations, leading to higher values of the HB energy in Fig. 16 as compared to the corresponding plots in Fig. 3.

The rapid dissipation of the stretching energy in stretching regime III, in which the axial buckling of the central part of the nanotube (e.g., Fig. 10) results in a sharp drop of the stretching energy [see Fig. 3(c)], is more difficult to reproduce in the mesoscopic model. With the hysteresis approach described in Sec. III B and parameterized to maximize the energy removed in each buckling cycle (choosing $|\varepsilon_{str}^{bcl-min}| = 0.0142$ ensures a maximum energy drop of $\Delta E_{str}^{bcl} = 0.6935$ eV/Å), the decay rate in Fig. 16(b) is still substantially lower than the one observed in the atomistic simulations [see Fig. 3(c)]. While most of the stretching energy dissipates within the first 5 ps of the atomistic simulation, the dissipation in the mesoscopic simulation is slower and takes approximately 40 ps. Although the hysteresis approach does allow for a relatively fast dissipation of the stretching energy, it is limited by the maximum energy drop in buckled segments ($\Delta E_{str}^{bcl} = 0.6935$ eV/Å) and cannot remove all of the energy that should be transferred to the heat bath in the first buckling cycle. The rate of the stretching energy dissipation can be further increased by decreasing the value of $|\varepsilon_{str}^{bcl-max}|$, which controls the size of the buckling region. In particular, a decrease of $|\varepsilon_{str}^{bcl-max}|$ from 0.45 to 0.1 results in a substantial increase in the rate of the stretching energy dissipation (see Fig. 17) which is closer to that predicted in the atomistic simulation. The size of the buckling region in this case, however, increases to approximately 16 nm, which is three times larger than the size of the buckling region observed in the atomistic simulations (see Fig. 10). In applications of the mesoscopic model in which representation of the ultrafast stretching energy dissipation upon buckling is critical, this artificial expansion of the effective buckling region could be an appropriate solution.

The slower dissipation of bending vibrations, as compared to stretching vibrations, makes parameterization of the mesoscopic description of the bending energy dissipation more straightforward. The energy plots shown in Fig. 18 for mesoscopic simulations of free bending vibrations performed for CNTs with an initial temperature of 568 K and initial
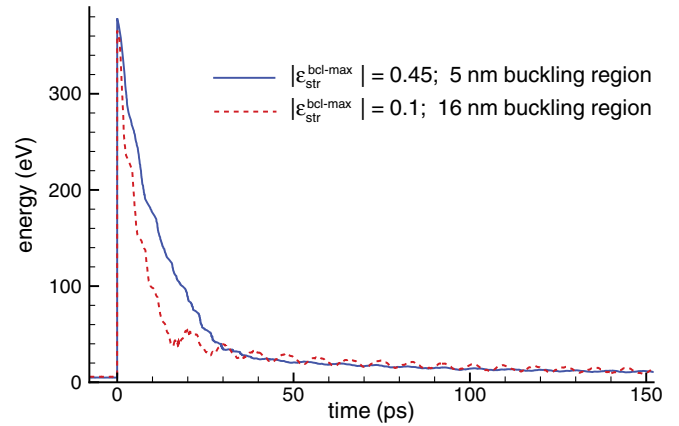

FIG. 17. (Color online) The evolution of the energies of the LA modes in simulations performed for the same conditions as in Fig. 16(b) with two values of $|\varepsilon_{str}^{bcl-max}|$, 0.45 and 0.1. The value of $\varepsilon_{str}^{bcl-max}$ defines the size of the buckling region, which is approximately 5 nm for $|\varepsilon_{str}^{bcl-max}| = 0.45$ and approximately 16 nm for $|\varepsilon_{str}^{bcl-max}| = 0.1$.

radii of curvature of 30 and 15 nm exhibit a good agreement with the corresponding plots obtained in atomistic simulations (see Fig. 12). The slow rate of the bending energy decay in Fig 18(a) is defined by weak damping forces added to reproduce the bending decay parameters given by Eq. (13) for bending regime I.

In bending regime II, the faster energy dissipation, shown in Fig. 18(b), is reproduced with the hysteresis approach. Preliminary test simulations revealed that, due to the small size of the CNT segments used in the mesoscopic simulations (2.6 Å), thermal fluctuations superimposed on the large-scale bending oscillations of the CNT lead to the generation of "thermal buckling" events, in which the local curvature transiently exceeds the critical value for buckling due to a thermal fluctuation. This effect of "thermal buckling" is not present when a larger segment length (e.g., 2 nm) is used in the mesoscopic simulations. To reduce the effect of thermal fluctuations on the energy dissipation rate, the hysteresis is only applied when the time in the buckled state (see Sec. III B) exceeds a predefined value, taken to be 100 fs in this work. With this adjustment, the choice of $R_{bnd}^{bcl-min} = 3.6$ nm (corresponding to an energy drop of $\Delta E_{bnd}^{bcl} = 0.026$ eV in each buckling cycle) is found to ensure the same duration of the first stage of the energy dissipation (approximately 50 ps) as observed in the atomistic simulation [see Fig. 12(b)]. After 50 ps the buckling kinks cease to appear, and the bending energy dissipation continues as in bending regime I.

The energy dissipation due to the hysteresis also quenches the thermal energy of the BA modes and, through dynamic coupling, the LA modes. This quenching, associated with both the loss of ΔE_{bnd}^{bcl} and the softening of the potential at R_{bnd}^{bcl} in each hysteresis cycle, manifests itself in a decrease of the stretching energy in Fig. 18(b) from its initial value, $E_{LA}^{\theta} = 5.18$ eV, down to 2.8 eV within 200 ps. The stretching energy then slowly recovers to the equilibrium value corresponding to the current HB temperature θ. The decrease of the thermal component of the bending energy is masked by the dominant contribution of the energy associated with low-frequency
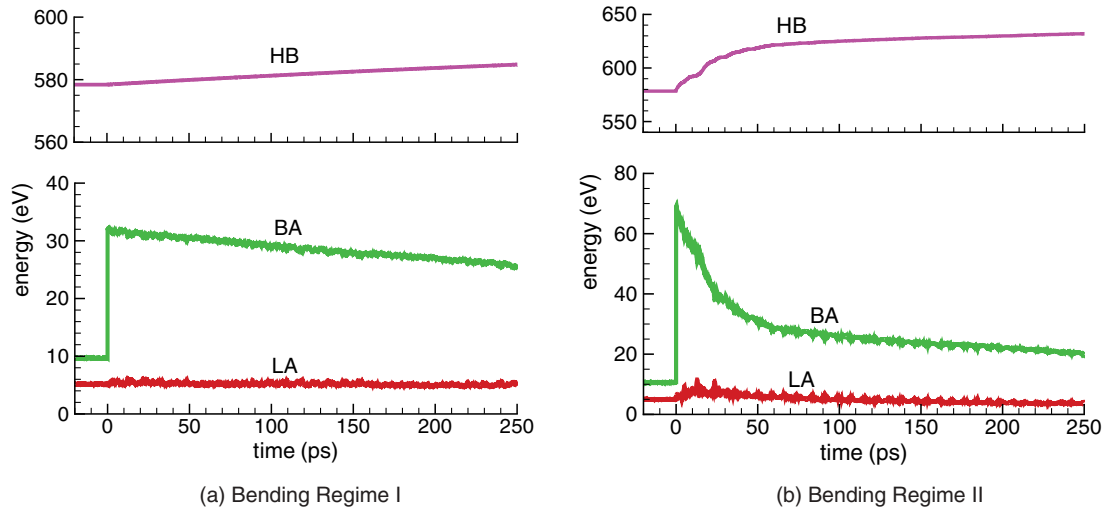
FIG. 18. (Color online) The evolution of the energies of the LA, BA, and HB modes in mesoscopic simulations performed for CNTs equilibrated at a temperature of 568 K and bent into an arc with a constant radius of curvature equal to 30 nm (a) and 15 nm (b) at time $t = 0$. The analogous plots for the atomistic simulations are shown in Figs. 12(a) and 12(b). In contrast to the atomistic simulations, the Rad modes are included within the HB modes in the mesoscopic simulations.

mechanical vibrations and is not apparent in Fig. 18(b). The delayed decrease of the energy of the LA modes, with respect to the duration of the bending buckling energy hysteresis regime, is explained by the finite time of dynamic equilibration between the thermal bending and stretching vibrations. Note that the effect of the strain energy hysteresis on the thermal vibrations associated with the BA and LA modes diminishes with increasing mesoscopic segment length and, in a simulation performed with 2-nm segments, the stretching energy does not decrease below its initial thermal value.

IV. SUMMARY

The rates and mechanisms of acoustic energy dissipation in CNTs were investigated in atomistic MD simulations performed for individual CNTs with different levels of initial stretching and bending deformation. The analysis of energy redistribution in simulations of free stretching and bending vibrations is based on the partitioning of the total energy of a CNT into contributions of the longitudinal, bending, radial, and remaining "heat bath" modes. This partitioning enables evaluation of the rates of mechanical energy dissipation and provides insights into the pathways and critical processes responsible for the redistribution of energy among the vibrational modes.

For stretching vibrations, the simulations reveal the existence of three distinct regimes of energy dissipation. At low levels of the initial excitation, in stretching regime I, a gradual decay of the energy of the excited LA modes is observed on the time scale of hundred(s) of picoseconds. For strong excitation, in stretching regime III, an immediate dissipation of a large part (75–95%) of the initial stretching energy occurs at a time scale comparable to one period of stretching oscillations. This fast thermalization of the stretching excitation is attributed to the formation of axial shell buckling kink(s) in the central part of the CNT, where the nanotube experiences strong transient compression due to the interaction of two unloading waves propagating from the free ends of the stretched nanotube. The

regimes of the gradual and immediate energy dissipation are separated by the intermediate stretching regime II, in which dynamic coupling between the longitudinal vibrational modes and the radial "squash" mode leads to delayed axial buckling followed by rapid energy transfer to the higher-frequency vibrational modes.

As in the case of stretching vibrations, the onset of buckling plays a prominent role in the damping of bending vibrations and leads to the identification of two distinct regimes of energy dissipation. In bending regime I, in the absence of bending buckling, very slow decay of bending oscillations occurs on the time scale of tens of nanoseconds. In bending regime II, in which the recurrent formation and relaxation of bending buckling kinks is observed, the energy of bending vibrations dissipates on the time scale of several periods of bending oscillations. In the absence of buckling, the rates of energy dissipation for both stretching and bending oscillations increase with increasing temperature and increasing excess energy of the corresponding vibrational modes. The dependencies of the decay rates on the temperature and the excess energy, predicted in the MD simulations for the LA and BA modes, are fitted to empirical relations and are used in the parameterization of a mesoscopic model capable of simulating systems consisting of a large number of interacting CNTs.

The mesoscopic model is advanced by adding a description of the energy exchange between the dynamic degrees of freedom of the mesoscopic model and the energy of the vibrational modes that are not explicitly represented in the model. Two complementary methods for the description of mechanical energy dissipation in the mesoscopic model are developed. The gradual dissipation of acoustic vibrations in the absence of buckling is described by adding a damping force to the equations of motion for the dynamic elements of the mesoscopic model. The computational description of the rapid dissipation of the energy of the LA and BA modes in the presence of buckling is based on strain energy hysteresis approach, which accounts for localized thermalization in the vicinity

of buckling kinks. The ability of the improved mesoscopic model to reproduce complex multistep processes of acoustic energy dissipation, as predicted in the atomistic simulations, is demonstrated in mesoscopic simulations of free stretching and bending vibrations of individual CNTs. The addition of the heat bath approach to the mesoscopic model extends the area of applicability of the model to dynamic phenomena involving fast mechanical energy deposition in CNT-based materials.

*Present address: Department of Chemistry, University of Cambridge, United Kingdom.

†Present address: Department of Chemical Engineering, Massachusetts Institute of Technology, USA.

‡Author to whom correspondence should be addressed: lz2n@virginia.edu

[1] Q. Cao and J. A. Rogers, Adv. Mater. **21**, 29 (2009).

[2] M. Zhang, S. Fang, A. A. Zakhidov, S. B. Lee, A. E. Aliev, C. D. Williams, K. R. Atkinson, and R. H. Baughman, Science **309**, 1215 (2005).

[3] T. Kashiwagi, F. Du, J. F. Douglas, K. I. Winey, R. H. Harris, Jr., and J. R. Shields, Nat. Mater. **4**, 928 (2005).

[4] B.-W. Jeong, J.-K. Lim, and S. B. Sinnott, J. Appl. Phys. **101**, 084309 (2007).

[5] D. Qi, J. Hinkley, and G. W. He, Model. Simul. Mater. Sci. **13**, 493 (2005).

[6] W. J. Evans and P. Keblinski, Nanotechnology **21**, 475704 (2010).

[7] L. V. Zhigilei, C. Wei, and D. Srivastava, Phys. Rev. B **71**, 165417 (2005).

[8] A. N. Volkov and L. V. Zhigilei, J. Phys. Chem. C **114**, 5513 (2010).

[9] M. J. Buehler, J. Mater. Res. **21**, 2855 (2006).

[10] S. W. Cranford and M. J. Buehler, Nanotechnology **21**, 265706 (2010).

[11] A. N. Volkov and L. V. Zhigilei, ACS Nano **4**, 6187 (2010).

[12] A. N. Volkov and L. V. Zhigilei, Phys. Rev. Lett. **104**, 215902 (2010).

[13] A. N. Volkov, T. Shiga, D. Nicholson, J. Shiomi, and L. V. Zhigilei, J. Appl. Phys. **111**, 053501 (2012).

[14] A. N. Volkov and L. V. Zhigilei, Appl. Phys. Lett. **101**, 043113 (2012).

[15] R. A. Jishi, L. Venkataraman, M. S. Dresselhaus, and G. Dresselhaus, Chem. Phys. Lett. **209**, 77 (1993).

[16] D. S. Ivanov and L. V. Zhigilei, Phys. Rev. B **68**, 064114 (2003).

[17] D. J. Phares and A. R. Srinivasa, J. Phys. Chem. A **108**, 6100 (2004).

[18] A. Strachan and B. L. Holian, Phys. Rev. Lett. **94**, 014301 (2005).

[19] S. T. Huxtable, D. G. Cahill, S. Shenogin, L. Xue, R. Ozisik, P. Barone, M. Usrey, M. S. Strano, G. Siddons, M. Shim, and P. Keblinski, Nat. Mater. **2**, 731 (2003).

[20] S. Shenogin, L. Xue, R. Ozisik, P. Keblinski, and D. G. Cahill, J. Appl. Phys. **95**, 8136 (2004).

[21] C. F. Carlborg, J. Shiomi, and S. Maruyama, Phys. Rev. B **78**, 205406 (2008).

[22] H. Jiang, M. F. Yu, B. Liu, and Y. Huang, Phys. Rev. Lett. **93**, 185501 (2004).

[23] S. Akita, S. Sawaya, and Y. Nakayama, Jpn. J. Appl. Phys. **46**, 6295 (2007).

[24] D. Danailov, P. Keblinski, S. Nayak, and P. M. Ajayan, J. Nanosci. Nanotechnology **2**, 503 (2002).

[25] P. A. Greaney, G. Lani, G. Cicero, and J. C. Grossman, Nano Lett. **9**, 3699 (2009).

[26] L. X. Benedict, S. G. Louie, and M. L. Cohen, Solid State Commun. **100**, 177 (1996).

[27] J. Hone, M. C. Llaguno, M. J. Biercuk, A. T. Johnson, B. Batlogg, Z. Benes, and J. E. Fischer, Appl. Phys. A **74**, 339 (2002).

[28] S. J. Stuart, A. B. Tutein, and J. A. Harrison, J. Chem. Phys. **112**, 6472 (2000).

[29] K. M. Liew, X. Q. He, and C. H. Wong, Acta Mater. **52**, 2521 (2004).

[30] J. Zhu, Z. Y. Pan, Y. X. Wang, L. Zhou, and Q. Jiang, Nanotechnology **18**, 275702 (2007).

[31] G. Cao and X. Chen, Phys. Rev. B **73**, 155435 (2006).

[32] There are two distinct contributions to the error in the calculation of the decay rates: a systematic error resulting from the finite width of the time intervals and a statistical error arising from the variations in the atomic trajectories across different simulations. The systematic contribution, approximated by the standard errors of regression, is minimized by the choice of time interval width. The error estimates used for fitting the rates and shown as error bars in the figures are the unbiased weighted standard deviations of simulation-averaged values, where the simulation averages are weighted according to the variances in parameters calculated by the linear regression in each time interval.

[33] Y. Y. Zhang, V. B. C. Tan, and C. M. Wang, J. Appl. Phys. **100**, 074304 (2006).

[34] B. Ni, S. B. Sinnott, P. T. Mikulski, and J. A. Harrison, Phys. Rev. Lett. **88**, 205505 (2002).

[35] J. Feliciano, C. Tang, Y. Zhang, and C. Chen, J. Appl. Phys. **109**, 084323 (2011).

[36] D. W. Brenner, O. A. Shenderova, J. A. Harrison, S. J. Stuart, B. Ni, and S. B. Sinnott, J. Phys.: Condens. Matter **14**, 783 (2002).

[37] A. N. Volkov, K. R. Simov, and L. V. Zhigilei, *Proceedings of the ASME International Mechanical Engineering Congress and Exposition*, ASME Paper No. IMECE2008-68021, pp. 1235-1245 (ASME, New York, NY, 2008).

[38] S. Berber, Y.-K. Kwon, and D. Tománek, Phys. Rev. Lett. **84**, 4613 (2000).

[39] S. Maruyama, Physica B **323**, 193 (2002).

[40] Q. Li, C. Liu, X. Wang, and S. Fan, Nanotechnology **20**, 145702 (2009).

[41] E. Pop, D. Mann, Q. Wang, K. Goodson, and H. Dai, Nano Lett. **6**, 96 (2006).

[42] A. Kutana and K. P. Giapis, Phys. Rev. Lett. **97**, 245501 (2006).